Geochemistry Geophysics Geosystems G3
AN ELECTRONIC JOURNAL OF THE EARTH SCIENCES
Published by AGU and the Geochemical Society

Article
Volume 9, Number 7
30 July 2008
Q07S08, doi:10.1029/2008GC001963
ISSN: 1525-2027

Seismic tomography and earthquake locations in the Nicaraguan and Costa Rican upper mantle

Ellen M. Syracuse
Department of Earth Sciences, Boston University, 675 Commonwealth Avenue, Room 141, Boston, Massachusetts 02215, USA (syracuse@bu.edu)

Geoffrey A. Abers
Lamont-Doherty Earth Observatory, P.O. Box 1000, 61 Route 9W, Palisades, New York 10964, USA

Karen Fischer
Department of Geological Sciences, Brown University, 324 Brook Street, Box 1846, Providence, Rhode Island 02912, USA

Laura MacKenzie
Department of Earth Sciences, Boston University, 675 Commonwealth Avenue, Room 141, Boston, Massachusetts 02215, USA

Catherine Rychert
Scripps Institution of Oceanography, Institute of Geophysics and Planetary Physics, University of California, San Diego, 9500 Gilman Drive, La Jolla, California 92093-0225, USA

Marino Protti and Víctor González
Observatorio Vulcanológico y Sismológico de Costa Rica, Universidad Nacional, Avenida 7, Calle 11, Heredia, Costa Rica

Wilfried Strauch
Instituto Nicaragüense de Estudios Territoriales, Postal Apdo. 2110, Managua, Nicaragua

[1] The Central American subduction zone exhibits large variations in geochemistry, downgoing plate roughness and dip, and volcano locations over a short distance along the arc. Results from joint inversions for *Vp*, *Vp*/*Vs*, and hypocenters from the Tomography Under Costa Rica and Nicaragua (TUCAN) experiment give insight into its geometry and structure. In both Costa Rica and Nicaragua, the intermediate-depth seismic zone is a single layer no more than 10 to 20 km thick. Tomographic images show that throughout Nicaragua and Costa Rica the slowest mantle *P* wave velocities appear below and behind the volcanic front, indicating likely zones of highest temperature extending 80 to 120 km depth. A sheet of high *Vp*/*Vs*, thought to be caused by melt, is imaged directly beneath the Nicaraguan volcanoes, whereas a weaker, broader anomaly is imaged beneath the Costa Rican volcanoes, potentially indicating a greater extent of melting beneath Nicaragua. Within the downgoing plate, anomalously low velocities occur at least 20–30 km below Wadati-Benioff zone seismicity, to depths of 140 km beneath Nicaragua and to 60 km depth beneath Costa Rica. They indicate 10–20% serpentinized upper mantle of the downgoing plate beneath Nicaragua, similar to that inferred from refraction seaward of the trench, but continuing to subarc depths. This unusually hydrated lithosphere may introduce more water into the Nicaraguan mantle, initiating increased amount of melting and fluid flux to the arc.

Components: 10,638 words, 15 figures.

Keywords: subduction; serpentine; melt; seismic velocities; slab.

Index Terms: 8180 Tectonophysics: Tomography (6982, 7270); 8170 Tectonophysics: Subduction zone processes (1031, 3060, 3613, 8413); 8185 Tectonophysics: Volcanic arcs.

Received 28 January 2008; **Revised** 5 May 2008; **Accepted** 9 May 2008; **Published** 30 July 2008.

Syracuse, E. M., G. A. Abers, K. Fischer, L. MacKenzie, C. Rychert, M. Protti, V. González, and W. Strauch (2008), Seismic tomography and earthquake locations in the Nicaraguan and Costa Rican upper mantle, *Geochem. Geophys. Geosyst.*, *9*, Q07S08, doi:10.1029/2008GC001963.

Theme: Central American Subduction System
Guest Editors: G. Alvarado, K. Hoernle, and E. Silver

1. Introduction

[2] Volcanism occurs at the vast majority of subduction zones, but the processes that drive magma generation are not well known. Variations in plate convergence velocity, slab dip, and slab age among different regions lead to several predicted thermal structures of the mantle wedge overlying the slab, and a large range in the geometry of melt transport [*Davies and Stevenson*, 1992; *England et al.*, 2004; *England and Wilkins*, 2004; *Syracuse and Abers*, 2006; *Cagnioncle et al.*, 2007]. The geochemistry of arc volcanoes also varies greatly between regions, implying differences in the amounts of fluid derived from the slab and slab-related sediments, degree of melting and location of melting [*Plank and Langmuir*, 1988, 1993].

[3] Seismic velocity tomography helps illuminate subduction zone structure and variations in temperature and fluid distribution. Velocities are sensitive to temperature through reduction of the bulk and shear moduli with increasing temperature [i.e., *Hacker and Abers*, 2004]. Melt or free water will also reduce seismic velocities in different ways, depending on pore geometries [*Takei*, 2002]. Serpentinization, caused by the addition of water to peridotite, will also reduce velocities, and is often cited as the cause of low *Vp*, high *Vp*/*Vs* anomalies in the cold mantle wedge corner [e.g., *Hyndman and Peacock*, 2003; *DeShon and Schwartz*, 2004]. If pervasive over large enough volumes, any of these variations will affect seismic velocities in a way that is detectable through body wave tomography.

[4] Southern Central America exhibits contrasts in subduction zone output over an along-arc distance as short as 500 km. Geochemical tracers in arc lavas thought to represent contributions from the downgoing slab and subducted sediment increase from near-MORB values in Costa Rica toward globally high levels in Nicaragua [*Patino et al.*, 2000]. For example, in Costa Rica, ^{10}Be concentrations are extremely low, while Nicaragua has the highest ^{10}Be concentration globally [*Morris et al.*, 1990]. Melt inclusions also indicate that there is up to two times more water in the source of Nicaraguan magmas than in Costa Rican ones [*Wade et al.*, 2006]. The incoming Cocos plate in Nicaragua shows extensive faulting at the outer rise, which may allow additional water to be incorporated as serpentine in the subducting mantle and released at depth [*Rüpke et al.*, 2002; *Ranero et al.*, 2003], an inference supported by oxygen isotope studies of Nicaraguan arc lavas [*Eiler et al.*, 2005]. Still, the evidence for deep volatile transport remains indirect, and the processes that control variations in melting are poorly understood.

[5] We use data from the Tomography Under Costa Rica and Nicaragua (TUCAN) experiment (Figure 1) to obtain a three-dimensional seismic velocity model in *Vp* and *Vp*/*Vs* for both Costa Rica and Nicaragua to 200 km depth. Changes in temperature, hydration, and the presence of melt have strong but differing effects on *Vp* and *Vp*/*Vs* [*Takei*, 2002; *Karato*, 2003]. We find low velocities in the subducted plate, more so beneath Nicaragua than Costa Rica, which may indicate hydration of the subducted crust and upper mantle to 150 km depth. A sheet of elevated *Vp*/*Vs* rises from the slab beneath the volcanoes in Nicaragua, supporting the possibility of localized region of melt vertically connecting the slab and the volcanoes.

2. Previous Seismic Studies

[6] Past seismic tomography in Costa Rica and Nicaragua has shown variations in the structure of

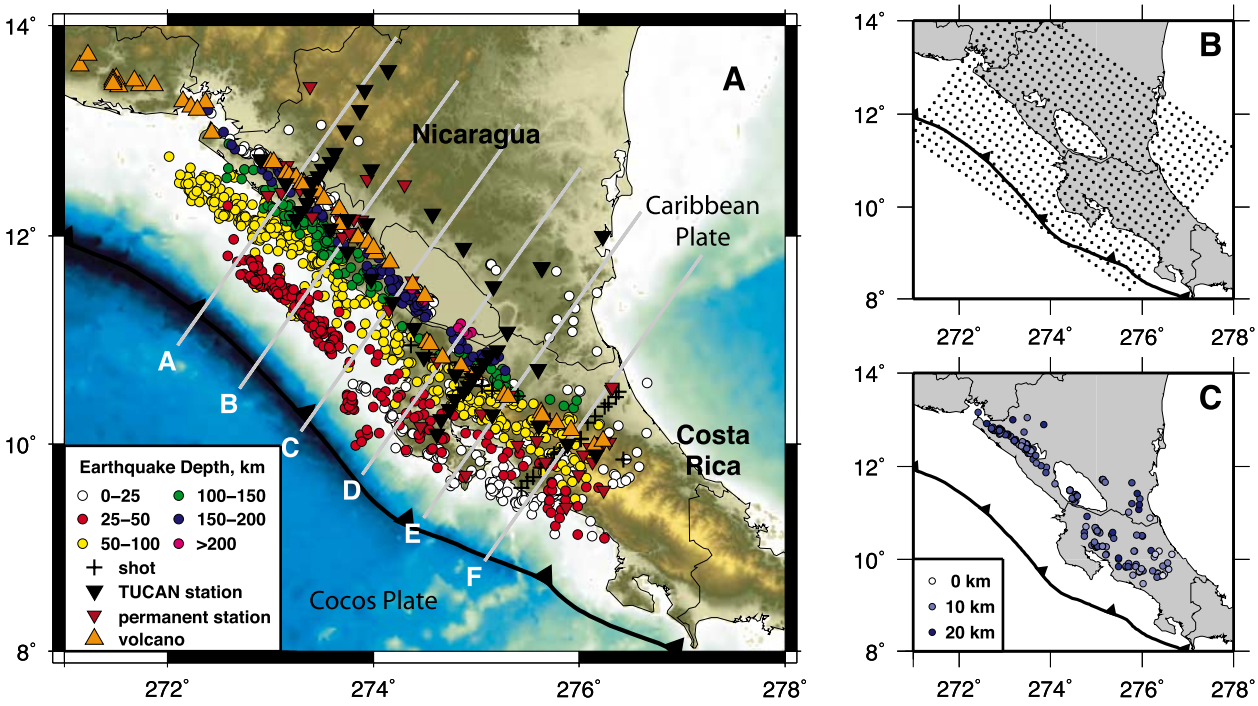

Figure 1. Figure 1a shows stations, seismicity, and shot locations (D. Lizarralde and S. Holbrook, personal communication, 2006) used in the inversion. The locations of the six cross sections referred to throughout the text and figures are indicated. Figure 1b shows the grid nodes used in the inversions. Figure 1c highlights the upper plate earthquakes. In all map views the sawtooth line indicates the location of the trench based on bathymetry.

the subduction zone, but studies have been limited in spatial extent and seismic velocity resolution is generally poor at depths greater than 50–100 km [*Protti et al.*, 1996; *Husen et al.*, 2003; *DeShon et al.*, 2006]. Data from both local and teleseismic earthquake catalogs show an increase from south to north in slab dip and the depth at which seismicity terminates, but the details differ (Figure 2). For example, local earthquake locations beneath Nicaragua indicate that the slab is near vertical and remains trenchward of the volcanic front [*Protti et al.*, 1994], whereas teleseismic earthquake locations [*Engdahl et al.*, 1998] indicate that the slab is on average 150 km beneath the volcanic front [*Syracuse and Abers*, 2006]. In Costa Rica, where network coverage has been better, differences between data sets are less [*Protti et al.*, 1994; *Husen et al.*, 2003].

[7] Three-dimensional (3-D) velocity tomography studies of this region have been largely focused on the *P* wave velocity structure of north and central Costa Rica. One one-dimensional (1-D) *P* wave velocity study samples the sediment layer at depths less than 2 km in central Nicaragua and to 50 km depth northern Costa Rica [*Matumoto et al.*, 1977], showing a 43 km thick crust in northern Costa Rica. *Protti et al.* [1996] produced a three-dimensional *P* wave velocity model for central Costa Rica with resolution to 50 km depth showing below-average crustal velocities (4.0 to 4.8 km/s) in the shallow crust beneath volcanoes and a high-velocity slab (6.8 to 7.2 km/s) at 20–30 km depth in the fore arc.

[8] Inversions extending to mantle depths have been mainly limited to the fore arc and have characterized the mantle wedge as a region of *P* wave velocities decreased to less than 7.0 km/s [*Husen et al.*, 2003] (6.8–7.0 km/s [*Husen et al.*, 2003; *DeShon and Schwartz*, 2004; *DeShon et al.*, 2006]). Additionally, low *P* wave velocities (~7.0 km/s) in parts of the slab beneath northwestern Costa Rica at depths around 30 km and deeper than 60 km [*Husen et al.*, 2003] have been attributed to a hydrated or gabbroic slab crust. *S* wave velocity analysis has been limited to two studies [*DeShon and Schwartz*, 2004; *DeShon et al.*, 2006] due to the predominance of vertical component seismometers in local networks. *DeShon et al.* [2006] find low *Vp* (6.8 to 7.0 km/s) and *Vp*/*Vs* of 1.73–1.78 in the mantle wedge, leading them to infer less than 10% serpentinization in the fore-arc mantle near the Nicoya Peninsula. Serpentine is characterized by unusually high *Vp*/*Vs* [*Christensen*, 1996] and has been proposed as a major store of water in fore arcs [*Hyndman and Peacock*, 2003].

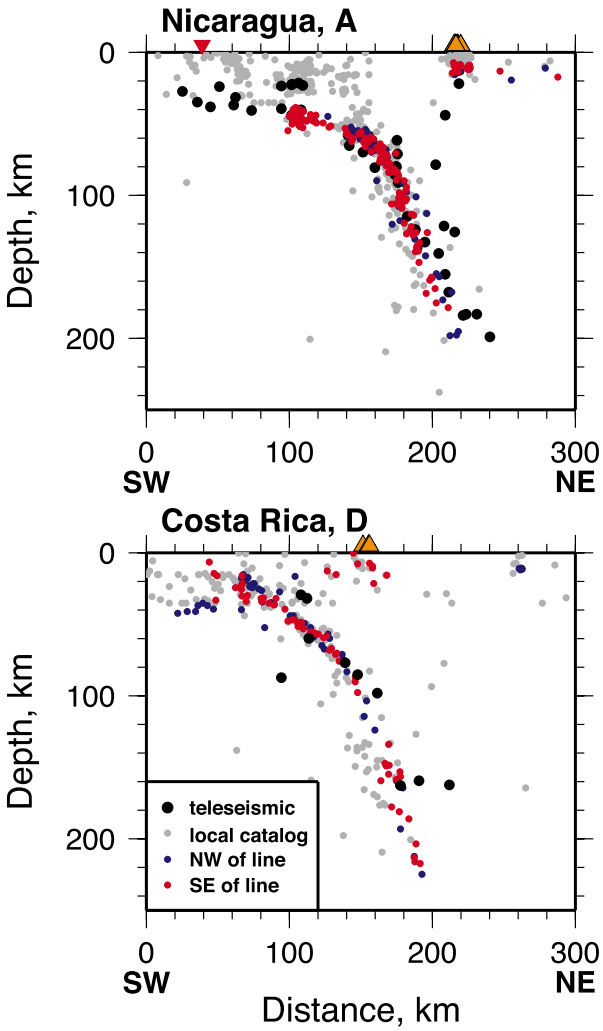

Figure 2. A comparison between seismicity relocated in this study (red and blue circles) and that of previous earthquake catalogs (black and gray circles). Hypocenters relocated in this study are separated into two groups relative to the projection line to highlight that some of the apparent width of the Wadati-Benioff zone is due to changes in slab position relative to the projection line, versus actual thickness of the Wadati-Benioff zone. Hypocenters from local catalogs (INETER catalog) [*Protti et al.*, 1994] are for the same earthquakes relocated in this study. Both local and teleseismic hypocenters [*Engdahl et al.*, 1998; *Syracuse and Abers*, 2006] show a thicker Wadati-Benioff zone than is seen from hypocenters relocated in this study. Depths and velocities for this and Figures 3–5 and 7–15 have been converted to a flattened earth [*Mueller*, 1971]. Volcanoes are shown as orange triangles and the trench is shown as red inverted triangles. See Figure 1 for the locations of cross sections A and D.

[9] Teleseismic 3-D *P* wave tomography has mainly focused on the structure of the slab. *Colombo et al.* [1997] image the slab as a positive velocity anomaly of up to 8% to 250 km depth with a subvertical dip in northern Costa Rica and tear in the slab leading to a shallower dip of about 60° in central Costa Rica, with no evidence for a subducted slab in southern Costa Rica. They also image a broad low-velocity region in the mantle directly above the slab in northern Costa Rica, possibly due to hydrated magmas and fluids. *Rogers et al.* [2002] interpret tomographic images of the slab and mantle wedge beneath Nicaragua and northern Central America from *Kárason and van der Hilst* [2001] as evidence for a detached slab at about 200–300 km depth. By this depth, most local seismicity in the region has ceased. They argue that the detachment may lead to induced mantle flow across the slab gap and cause uplift of the overlying Caribbean plate. However, it is unclear how well the slab is actually sampled, since there are few nearby stations and the slab tear is below the seismicity.

[10] Receiver functions show thick crust in the Nicaraguan back arc (44 km thick) and the Costa Rican arc (38 km thick), and thinner crust beneath the arc in Nicaragua (25 km thick), perhaps due to crustal extension and thinning in Nicaragua [*MacKenzie et al.*, 2008]. Reduced amplitudes from Moho conversions beneath the arc and fore arc suggest the presence of fluids or melt in both Nicaragua and Costa Rica.

3. Data

[11] The TUCAN array consists of 47 PASSCAL broadband stations operating from July 2004 through March 2006 (Figure 1). Most stations were distributed in four lines from northern Nicaragua to central Costa Rica. Data at all stations were recorded continuously at 50 sps. Disks containing data were collected roughly monthly by members of OVSICORI-UNA (Observatorio Vulcanológico y Sismológico de Costa Rica, Universidad Nacional) and INETER (Instituto Nicargüense de Estudios Territoriales) and sent to Boston University, where they were reformatted and submitted to the IRIS Data Management Center.

[12] Waveforms corresponding to earthquakes recorded in catalogs from OVSICORI-UNA and INETER are analyzed by eye to identify earthquakes having at least 9 visible *P* arrivals and 1 *S* arrival that are recorded at TUCAN stations. Prior

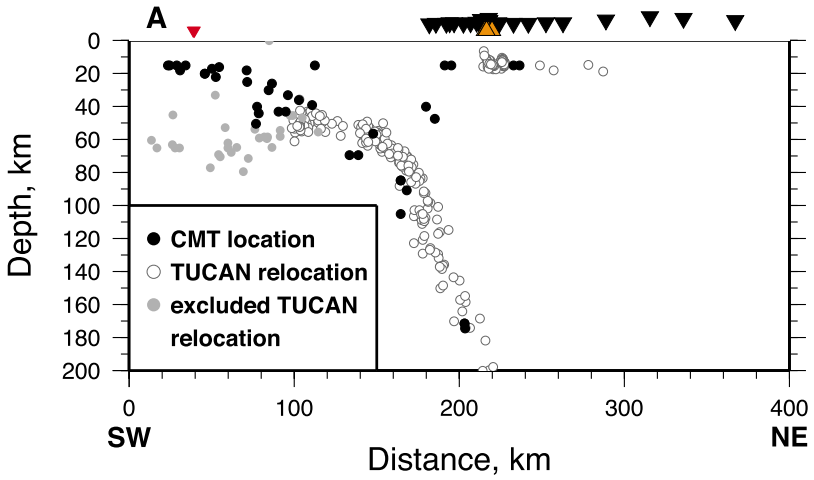

Figure 3. A comparison of relocations in the final 3-D velocity model with CMT hypocenters [*Dziewonski et al.*, 1981]. Note the discrepancies in the location of thrust earthquakes near the trench between the CMT locations and ours. Earthquakes that did not meet the minimum distance to a station are indicated in gray. See Figure 1 for the location of cross section A. Volcanoes are shown as orange triangles, stations are shown as black inverted triangles, and the trench is shown as red inverted triangles.

to picking, waveforms are filtered to correct the FIR filters to causal onsets [*Scherbaum*, 2002]. *P* and *S* arrivals are picked using a semiautomated autoregressive onset estimator based on *Pisarenko et al.* [1987] including uncertainties (S. Roecker, personal communication, 2000). Blunders in arrivals and uncertainties are corrected by hand. In cases where the *S* waves show differences between components, the earlier horizontal-component arrival is picked. Assuming the effects of shear wave splitting contribute an average *S* wave travel time split of 0.3 s [*Abt et al.*, 2006] and the average *S* wave travel time is 33 s, picking the earlier arrival leads to a maximum bias of *Vp*/*Vs* of 0.5% relative to isotropic velocities, compared with 3–7% variations estimated from inversion. *P* arrivals are picked from the vertical components. Additional *P* arrivals from the OVSICORI-UNA and INETER catalogs are also included, adding data from 48 stations, after network timing corrections are estimated and accounted for.

[13] For several earthquakes in the thrust zone offshore of Nicaragua there are large (>60 km) discrepancies in hypocenter depth between our initial locations and those from previous data sets such as the INETER catalogs and the CMT catalog [*Dziewonski et al.*, 1981] (Figure 3). We suspect this results from the lack of offshore stations. We impose a restriction that all earthquakes used in inversions must have at least one arrival from a station within 0.75° of the earthquake in initial locations, removing the earthquakes for which there are the discrepancies in depth of more than 20 km compared to slab seismicity from the CMT catalog, and thus eliminating the influence of these poorly constrained offshore hypocenters and downgoing raypaths. Smaller discrepancies also exist between our initial locations and those from teleseismic locations, but those can largely be attributed to systematic biases of teleseismic hypocenters often associated with subduction zones [*McLaren and Frohlich*, 1985; *van der Hilst and Engdahl*, 1992; *Syracuse et al.*, 2007]. This resulting data set contains 1348 earthquakes, 30970 *P* arrivals, and 11833 *S* arrivals. These data are supplemented by arrivals at TUCAN stations from 27 shots in central and northern Costa Rica from February and July 2005 (D. Lizarralde and S. Holbrook, personal communication, 2006), contributing an additional 307 *P* arrivals and 120 *S* arrivals (Figure 1).

4. Velocity Inversion Methods

[14] We use the method of *Roecker et al.* [2006], summarized here, to invert *P* and *S* arrival times for hypocenters and three-dimensional variations in velocities. The sample volume is parameterized as a 640 km × 420 km Cartesian grid with axes rotated 35° clockwise from North, extending to 300 km depth with velocity node spacing of 20 km. We calculate travel times from each point in the volume to each station by using a finite difference solution to the eikonal equation [*Hole and Zelt*, 1995; *Vidale*, 1990] calculated at 5 km grid spacing. These calculations also provide velocity deriv-

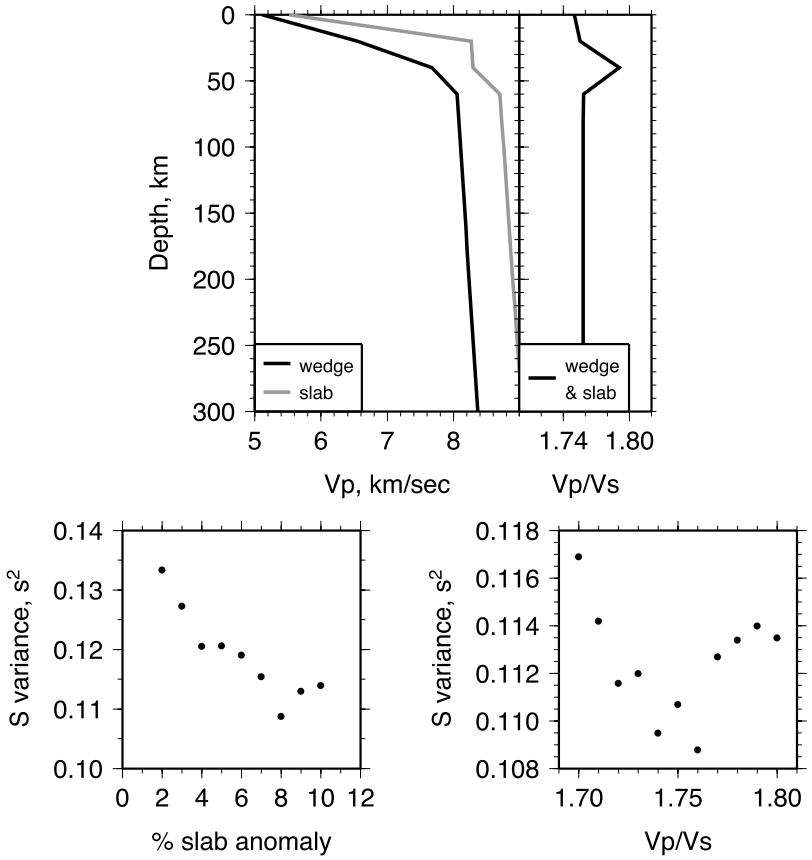

Figure 4. Initial *Vp* and *Vp*/*Vs* models from 1-D inversion. The black line shows the initial *P* wave velocities within the crust and mantle wedge. The gray line shows the initial *P* wave velocities within the slab, where velocities have been increased by 8%, and the Moho has been made shallower to accommodate for oceanic crust. *Vp*/*Vs* remains constant at a given depth within the slab and the mantle. The bottom left panel shows the variance of *S* arrivals for earthquakes greater than 100 km depth as a function of percentage of velocity increase within the slab using the above mantle wedge velocity model. The bottom right panel shows the variance of *S* arrivals for the same earthquakes as a function of mantle *Vp*/*Vs* with an 8% slab anomaly.

atives and allow fully nonlinear hypocenter estimates, to high precision when supplemented by a mesh-refining algorithm [*Roecker et al.*, 2006].

[15] Our initial velocity model is derived from a separate 1-D joint inversion for hypocenters, *P* wave slowness (reciprocal of *P* velocity) and *Vp*/*Vs*, solving for 10–20 km thick layers of constant velocity to 50 km depth, and a half-space below 50 km depth. Since the velocity model is more sensitive to *P* velocities than *S* velocities, eleven 1-D inversions are completed in which *Vp*/*Vs* is held fixed below 70 km depth at a range of values between 1.70 and 1.80. The resulting velocity models are interpolated to vertical nodes, and corrected to Cartesian coordinates via an Earth-flattening transform [*Mueller*, 1971]. A 3-D velocity model is created by adding an 8% fast slab to the 1-D model (based on the results of *Colombo et al.* [1997]) whose top surface is defined by the preliminary earthquake locations. Though greater than other estimates of slab velocities relative to background mantle velocities [*Lay*, 1997], the elevated slab velocity helps replicate realistic velocity gradients at the top of the slab. Hypocenters are then calculated in this slab velocity model, discarding all arrivals with travel time residuals greater than 1 s. The variance of travel time residuals is calculated for each velocity model, and the model that best fits the *S* arrivals from earthquakes whose hypocenters are greater than 100 km depth is chosen as the starting model (Figure 4). A similar test is completed for the resulting best fit 1-D plus slab model, in which the magnitude of the slab anomaly is varied from 2% to 10% faster than surrounding mantle. This test shows that a 8% fast anomaly in the slab best fits the *S* data (Figure 4); *P* data show less effect.

[16] Each iteration of the inversion is linearized in the standard manner [*Menke*, 1984], with the forward model approximated as

$$\mathbf{Gm} = \begin{bmatrix} \mathbf{H} & \mathbf{S} \\ \mathbf{0} & \mu\mathbf{D} \end{bmatrix} \begin{bmatrix} \mathbf{h} \\ \mathbf{s} \end{bmatrix} = \begin{bmatrix} \mathbf{d} \\ \mathbf{0} \end{bmatrix},$$

where **G** represents the matrix being inverted and m are model parameters. **G** consists of submatrices **H** containing hypocenter derivatives, **S** containing *P* wave slowness and *Vp*/*Vs* derivatives, and **D** containing smoothing constraints scaled by a scalar μ to provide stability. The model parameter vector **m** contains subvectors **h** containing hypocenter perturbations and **s** containing *P* wave slowness and *Vp*/*Vs* perturbations. The vector **d** contains travel time residuals [*Menke*, 1984]. The matrix **G** is inverted in the damped least squares sense with a LSQR inversion [*Paige and Saunders*, 1982], so it includes minimum-length damping whose damper is determined from a tradeoff curve between model length and misfit [*Menke*, 1984].

[17] Hypocenter derivatives are included in the inverse problem in order to not bias results to the initial hypocenters [*Thurber*, 1992; *Roecker et al.*, 2006]. The locations and origin times of shots are held fixed. In practice, updated hypocenters are calculated explicitly in the new velocity model using the full grid search, rather than using the approximate linearized perturbations.

[18] The smoothing submatrix, **D**, constrains the roughness of the inverted model by minimizing the gradients in slowness or *Vp*/*Vs* between neighboring grid nodes following *Menke* [1984]. The smoothness constant is scaled by the factor μ, which we choose to be 5000 for the *P* wave slownesses and 1000 for *Vp*/*Vs*, such that the norm of $\mathbf{s}^T\mathbf{D}^T\mathbf{Ds}$ is of similar size for both *P* wave slowness and *Vp*/*Vs*, and the model length is at least 10% smaller than if no smoothing is applied.

[19] Data and model uncertainties are accounted for in a variety of ways. Travel time residuals and corresponding rows of **G** are weighted by $1/\sigma_i$ where σ_i is the travel time uncertainty for the *i*th observation, incorporating an assumed 0.1 s uncertainty in theory, following *Tarantola and Valette* [1982]. The derivatives in **G** are also scaled by estimated a priori uncertainties in parameters, in part to correct for differences in scale between hypocenter, *P* wave slowness and *Vp*/*Vs* derivatives [e.g., *Tarantola*, 1986]. Relative to *P* wave slowness derivatives, hypocenter derivatives are multiplied by 100, based on the ratio between 0.1 s/km uncertainty in initial *P* wave slowness and 10 km uncertainty in initial earthquake location. The *Vp*/*Vs* derivatives are scaled by 10 to account for differences between units of *P* wave slowness and *Vp*/*Vs* perturbations.

[20] A total of five iterations are completed; with further iterations, the misfit to the *S* wave arrival times begins to increase. The first two iterations are overdamped using a damping value that is 10 times greater than the optimal value, in order to speed initial convergence. For subsequent iterations we use a damper determined from the misfit-model length tradeoff curve. Station corrections are calculated after the fourth iteration and are included in the final iteration to account for near-surface velocity anomalies at a spatial scale that is smaller than that resolvable by the station and grid spacing. The overall data variance is reduced from 0.0801 s^2 in the initial 1-D model including a slab to 0.0430 s^2 in the final 3-D model, with a misfit χ^2 value of 1.55 for *P* waves and 0.83 for *S* waves, indicating that the inversions explain the data to within uncertainties.

[21] All *Vp* values and hypocenters shown here are from inversions using the full data set, whereas the *Vp*/*Vs* results are from a separate inversion in which only raypaths with both *P* and *S* arrivals are included. While this limits our *Vp*/*Vs* data set to 21414 *P* and *S* arrivals, it prevents differences in *P* and *S* resolution from being mapped as *Vp*/*Vs* anomalies [*Saltzer et al.*, 2001].

5. Resolution Estimates

[22] In order to assess the spatial and amplitude recovery of our data, we use two types of tests: a checkerboard test [*Zelt*, 1998] and a variety of recovery tests for anomalies resembling features that are seen in the actual tomographic results. The checkerboard test has the advantage of giving a spatially uniform estimate of resolution throughout the volume at different length scales. However, the final result is susceptible to smearing along diagonals, suppressing horizontal and vertical smearing, and requires separate tests at different scales.

[23] All resolution tests are conducted in the same manner. A synthetic velocity model is created by adding perturbations to the *Vp* and/or *Vp*/*Vs* part of the initial velocity model. Synthetic arrival time data is created for the final set of relocated hypocenters and shots by finite difference. Gaussian random noise proportional to travel time uncertainties is

added to synthetic arrival times. After synthetic travel times are calculated for the perturbed velocity models, they are inverted once using the same parameters as in the actual inversions.

[24] For the checkerboard tests, two cell sizes are tested, 80 km and 40 km. *P* wave velocity anomalies are perturbed between −0.5 km/s and +0.5 km/s from the initial 1-D velocity model plus slab. *Vp*/*Vs* ratios are perturbed between −0.08 and +0.08 from the initial *Vp*/*Vs* model. Velocities vary sinusoidally laterally and with depth. Semblance, a measure of the similarity between the recovered and input models, is calculated for all points within the grid. A semblance value of at least 0.7 is considered to indicate a well-recovered portion of the model [*Zelt*, 1998]. However, the semblance may also be sensitive to the exact locations of positive and negative anomalies, so all results figures are shown with the region sampled by 50 or more raypaths highlighted, not the region of high semblance.

[25] The 80 km cell size model shows good recovery of *Vp* anomalies between the earthquakes and stations to 140–160 km depth for cross sections A through D (Figure 5; cross section locations on Figure 1). These cross sections also show good resolution as deep as 40 km below seismicity, due to long raypaths within the slab from earthquakes in different parts of the model. Cross-sections E and F display less resolution at larger depth, with a semblance value of 0.7 extending to 80–100 km depth beneath the volcanic front. At 40 km wavelength, the region of well-resolved *Vp*/*Vs* extends to 100–120 km depth beneath cross sections A through D, with resolution to 10–40 km below the slab surface. *Vp*/*Vs* resolution decreases to the southeast, with resolution within the wedge extending to 80 km depth in cross section E, and no well-resolved region in cross section F.

[26] The 40 km cell test shows that *Vp* anomalies of this size are only resolvable shallower than 80 km depth in the center of the mantle wedge for cross sections A through D. Anomalies of this size cannot be recovered in cross sections E and F, and nowhere can *Vp*/*Vs* anomalies of this size be recovered satisfactorily. Other recovery tests are discussed in the Results section.

6. Results

6.1. Hypocenters

[27] We observe that the maximum depth of seismicity occurs at 220–230 km depth near the Nicaragua-Costa Rica boundary, and shallows to 100 km depth near the end of the volcanic front in central Costa Rica (10°N), consistent with longer-duration studies [*Protti et al.*, 1994]. Upper-plate seismicity occurs predominantly within the volcanic front in Nicaragua, with 95% of earthquakes between 9 km and 17 km depth, and is more diffusely distributed in Costa Rica, extending from the fore arc to 140 km behind the arc, with 95% of earthquakes between 2 and 16 km depth (Figure 1).

[28] Relocations from this study show a Wadati-Benioff zone (WBZ) that is 12–19 km thick on average depending on the location (Figure 2), part of which could reflect scatter due to hypocentral errors. Previous analyses of Central American earthquakes have shown a Wadati-Benioff zone as wide as 40 km thickness throughout the subduction zone [*Protti et al.*, 1994; *Syracuse and Abers*, 2006], or as narrow as less than 20 km after relocation [*Husen et al.*, 2003].

[29] Errors in earthquake locations are determined for each earthquake by calculating the probability density function (PDF) of hypocentral coordinates in a cube that is centered on the hypocenter. The PDF describes the probability that an earthquake occurred at any given location assuming travel time errors and uncertainties described above [*Tarantola and Valette*, 1982]. The marginal PDF and 90% confidence interval is calculated in the *x*, *y*, and *z* directions in the grid, corresponding to the across arc, along arc, and vertical directions, respectively; their Pythagorean average is reported. In the 50–100 km depth range, the median uncertainty ranges from 1.7 to 2.8 km; in the 100–150 km depth range, the median uncertainty ranges from to 2.2 to 3.6 km; in the 150–200 km depth range, the median uncertainty ranges from 3.0 to 3.8 km. Within the upper plate in Nicaragua, 95% of earthquakes have uncertainties in all directions between 0.5 and 2.1 km. For Costa Rica, the formal errors range from 0.6 to 4.3 km, with similar vertical and horizontal uncertainties. In all cases, the uncertainties decrease toward the center of the array. Given these uncertainties and their potential contribution to widen the apparent thickness of the Wadati-Benioff zone, it is possible that the actual thickness of the Wadati-Benioff zone is as narrow as 2–10 km wide, whereas hypocenters from local catalogs [e.g., *Protti et al.*, 1996] for the same earthquakes show a much larger thickness.

[30] Hypocenters in this study show little change in overall slab geometry across the region between 10.5° N latitude and northwest Nicaragua, despite a

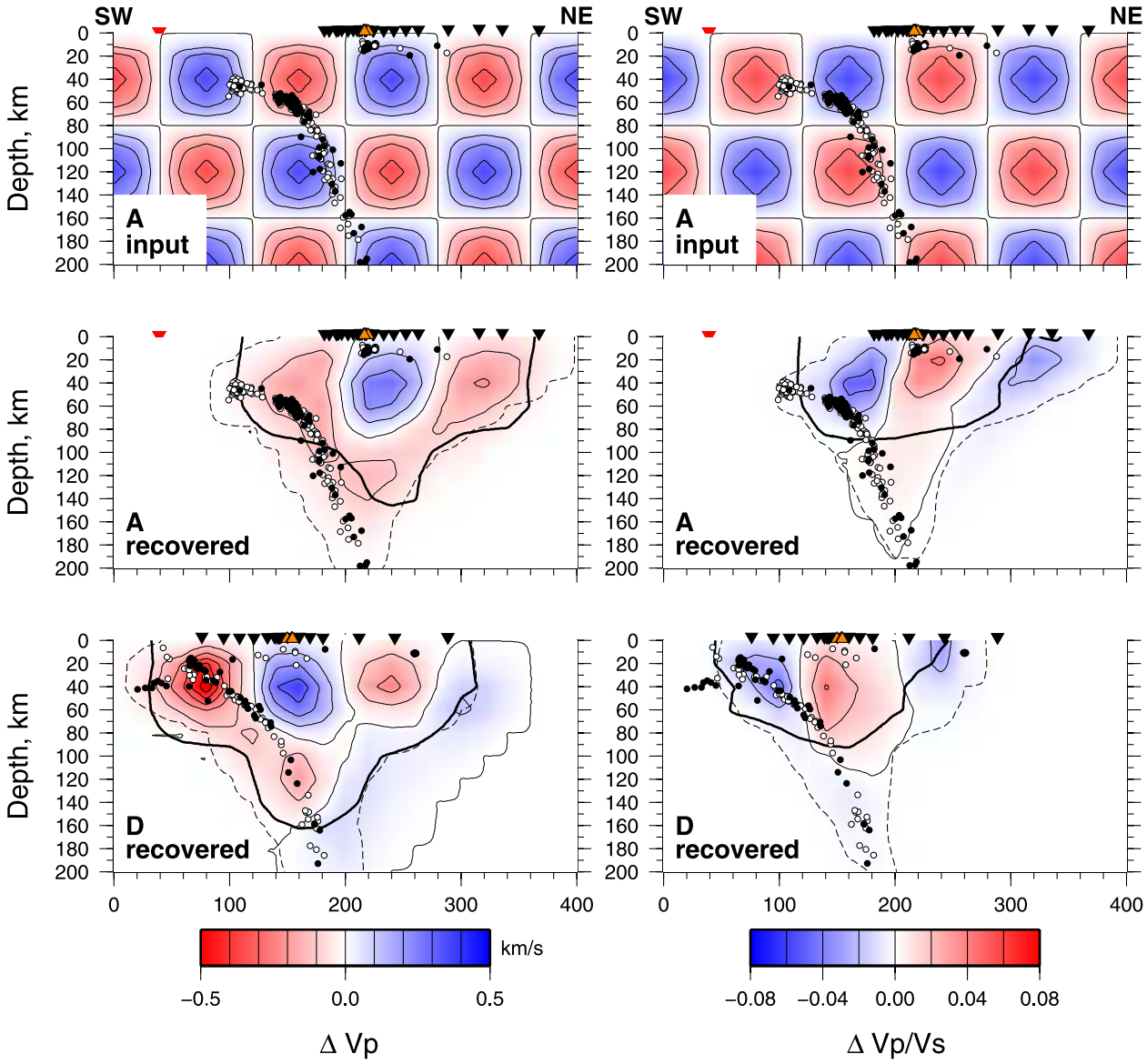

Figure 5. Checkerboard test inputs and recovered velocity models for an 80 km cell size: *Vp* input anomalies with respect to the initial 1-D velocity model plus slab (top left) and recovered model (middle and bottom left), and *Vp*/*Vs* input anomalies with respect to the initial 1-D *Vp*/*Vs* model and recovered model (top right) and recovered model (middle and bottom right). Note that the input checkerboard for cross section D has opposite values of that shown in the top panels. The thick black line represents the 0.7 semblance value contour, and the dashed line outlines the region sampled by 50 or more raypaths. The region within either of these contours is considered to be well resolved. Earthquakes projected 40 km to the northwest of each cross section line are shown in white, and those within 40 km to the southeast are shown in black. Symbols same as Figure 3.

large step in arc location. At the shift in the volcanic front at 11°N, there is no more than a 5–10 km shift in slab position and no change in slab dip (Figure 6). Given the hypocentral errors, a larger contortion in the slab would be seen if it were present. Further southeast (~84.5°W), there is evidence supporting the existence of a slab tear or change in slab dip, previously identified as the Quesada Sharp Contortion [*Protti et al.*, 1994], though the sharpness of this contortion cannot be resolved due to the limited data set in the area.

6.2. Tomographic Results

[31] The inversions show three systematic features: reduced velocities beneath and behind the volcanic front extending to depths as great as 140 km, a slow layer deep within the downgoing slab beneath

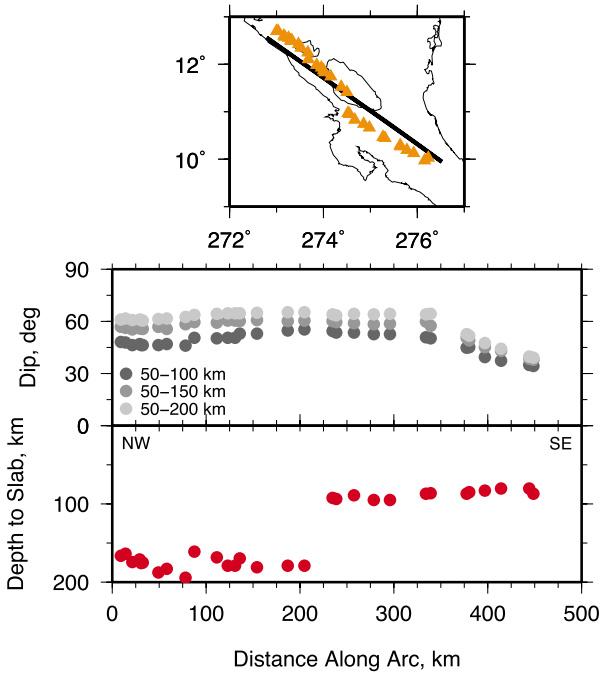

Figure 6. Plots of average slab dip and depth to the top of the Wadati-Benioff zone, along the volcanic front, updated from *Syracuse and Abers* [2006] using data in this study. Slab dips are calculated as the average dip between 50 and 100 km depth, 50 and 150 km depth, or 50 and 200 km depth as labeled. Location of section is shown in top panel, along with arc volcanoes (triangles).

Nicaragua from the surface to 80–140 km depth, and a vertically oriented sheet of high *Vp*/*Vs* in the mantle wedge beneath the Nicaraguan volcanoes (Figures 7, 8, 9, and 10). Each is discussed in detail below. The *Vp* model is shown as absolute velocities and the *Vp*/*Vs* model is shown as perturbations to the 1-D starting *Vp*/*Vs* model, because vertical changes in the initial 1-D model dominate absolute *Vp*/*Vs* values.

6.2.1. Wedge *Vp*

[32] The *Vp* model shows velocities of 7.6–8.2 km/s at 60–160 km depth in the mantle wedge beneath and behind the volcanic front in Nicaragua and Costa Rica, similar to what is seen in most other subduction zones [*Gorbatov et al.*, 1999; *Nakajima et al.*, 2001; *Conder and Wiens*, 2006; *Reyners et al.*, 2006; *Zhao et al.*, 2007] (Figures 7 and 9). The trenchward edge of the low-velocity region follows the 40 km jump in the volcanic front location at the Nicaragua-Costa Rica border. Reduced velocities (7.1–8.0 km/s) also exist in some parts of the fore-arc wedge between 40 and 60 km depth, in the same areas that a "cold nose" is observed in attenuation results (C. A. Rychert et al., Strong along-arc variation in attenuation in the mantle wedge beneath Costa Rica and Nicaragua, submitted to *Geochemistry, Geophysics, Geosystems*, 2008).

[33] A synthetic recovery test compares the observed low wedge velocities to what might be caused by a broad temperature anomaly (Figure 11). The wedge is simulated as a −0.35 km/s *P* wave velocity anomaly and a +0.05 *Vp*/*Vs* anomaly, based on that predicted for a +300°C temperature anomaly with a starting temperature of 1200°C and 5 mm grain size [*Faul and Jackson*, 2005]. The results of three inversions, completed as described in section 5, show average recoveries in regions sampled by 50 or more rays are 100% at 60 km depth in Nicaragua, 85% (0.3 km/s) at 60 km depth in Costa Rica, and 85% (0.3 km/s) at 80 and 100 km depth in both countries. Thus, the higher absolute *Vp* values beneath central Costa Rica in the actual tomographic model is not likely to be due to varying resolution along the arc.

6.2.2. *Vp*/*Vs*

[34] A sheet of elevated *Vp*/*Vs* extends to 140 km depth beneath the volcanic front in Nicaragua (Figures 8 and 10), with a maximum mantle *Vp*/*Vs* value of 1.80, compared to 1.76 in the 1-D starting model. At the Nicaragua-Costa Rica border, the distinct high *Vp*/*Vs* region transitions to shallower, broader areas of positive *Vp*/*Vs* anomalies beneath the arc in Costa Rica. Central Costa Rica shows poor resolution below 80 km depth. Low *Vp*/*Vs* (1.68–1.74) is observed in the Nicaraguan slab, as well as regions of low *Vp*/*Vs* (1.72–1.74) in the Nicaraguan fore-arc wedge.

[35] To test the extent to which resolution influences the slope of the positive anomaly, two end-member velocity models are tested (Figure 11). For a model in which the entire mantle wedge has a positive *Vp*/*Vs* anomaly of 0.05 (1.81 versus 1.76 mantle background), a broad region of elevated *Vp*/*Vs* that extends into the back arc is recovered. A model with a 40–50 km wide sheet of a positive *Vp*/*Vs* anomaly of 0.07 (1.83 versus 1.76 mantle background) that follows the volcanic front is also tested. Three iterations are completed for these tests to account for focusing effects. Beneath the volcanic front, similar amplitudes are recovered for both tests, but in the back-arc mantle, the recovered anomalies are distinct between the two input models. Thus, the data can distinguish a

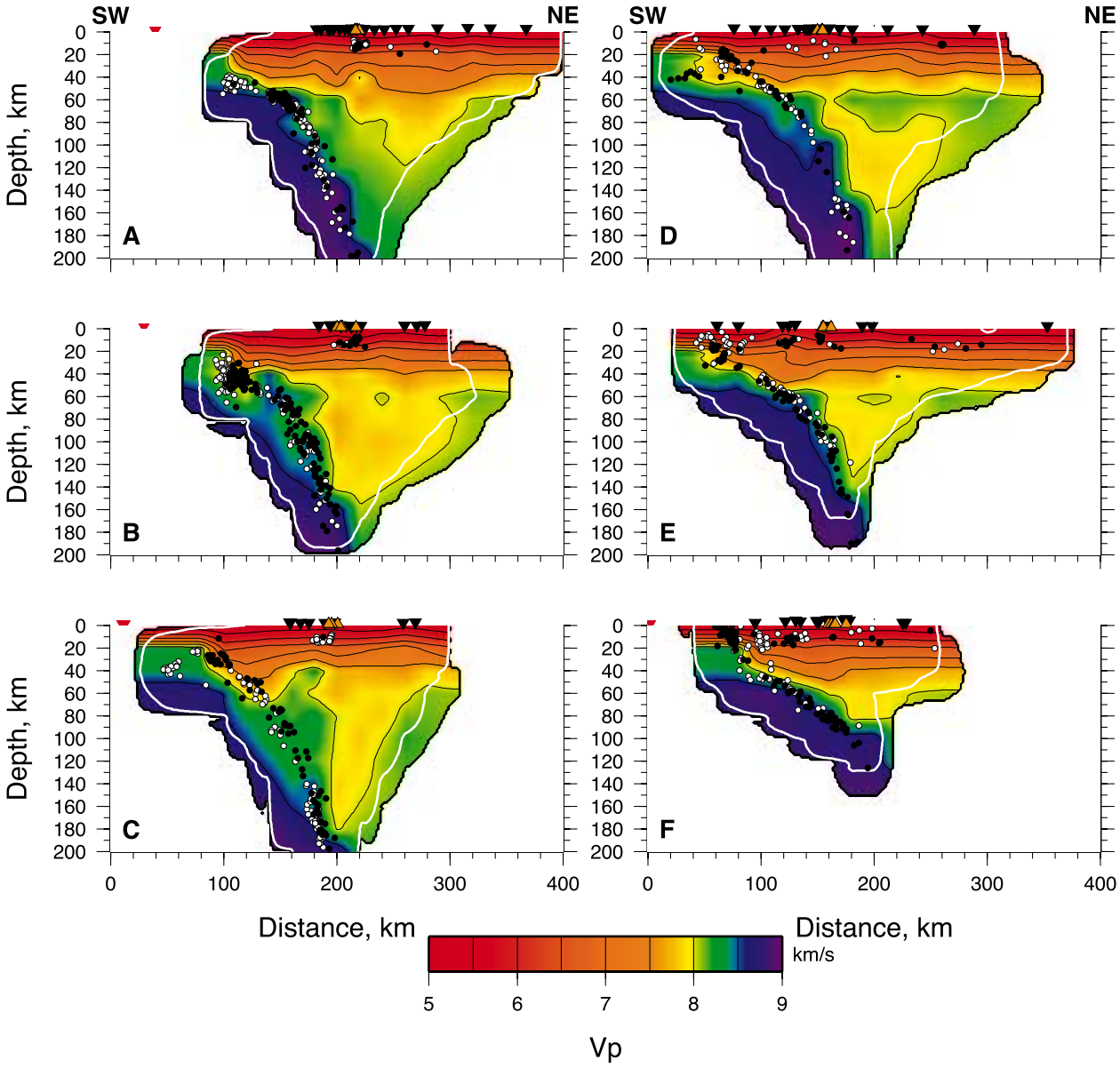

Figure 7. Cross sections through the final *P* wave velocity model. The model is shown for regions of the grid containing 10 or more rays, with the white contour surrounding regions containing 50 or more rays. Earthquakes projected 40 km to the northwest of each cross section line are shown in white, and those within 40 km to the southeast are shown in black. The location of the trench is shown with red inverted triangles. Depths and velocities are earth-flattened [*Mueller*, 1971]. See Figure 1 for the locations of cross sections. Symbols same as Figure 3.

sheet of elevated *Vp*/*Vs* from a broader region of elevated *Vp*/*Vs*. Recovery of the synthetic anomaly varies from 20% to 100% (1.77 to 1.83) along the Nicaraguan arc, indicating that the strength of the anomaly in that area may be in part due to better resolution. However, in central Costa Rica, 40% to 80% of the anomaly is recovered, similar to Nicaragua, indicating that the overall lack of an observed high *Vp*/*Vs* region beneath the arc in Costa Rica is robust (Figure 12).

6.2.3. Slab Velocity

[36] Decreased *P* wave velocities (4 to 6%) are recovered in the top of the slab beneath Nicaragua, despite the likely low temperatures there and the inclusion a fast slab with velocities of increased by 8% from the 1-D reference model (Figures 7 and 9). Note that the absolute velocity is dependent in the magnitude of the initial slab anomaly, but the percentage of decrease in velocity is robust, as indicated by tests with a 5% fast slab. The slab is

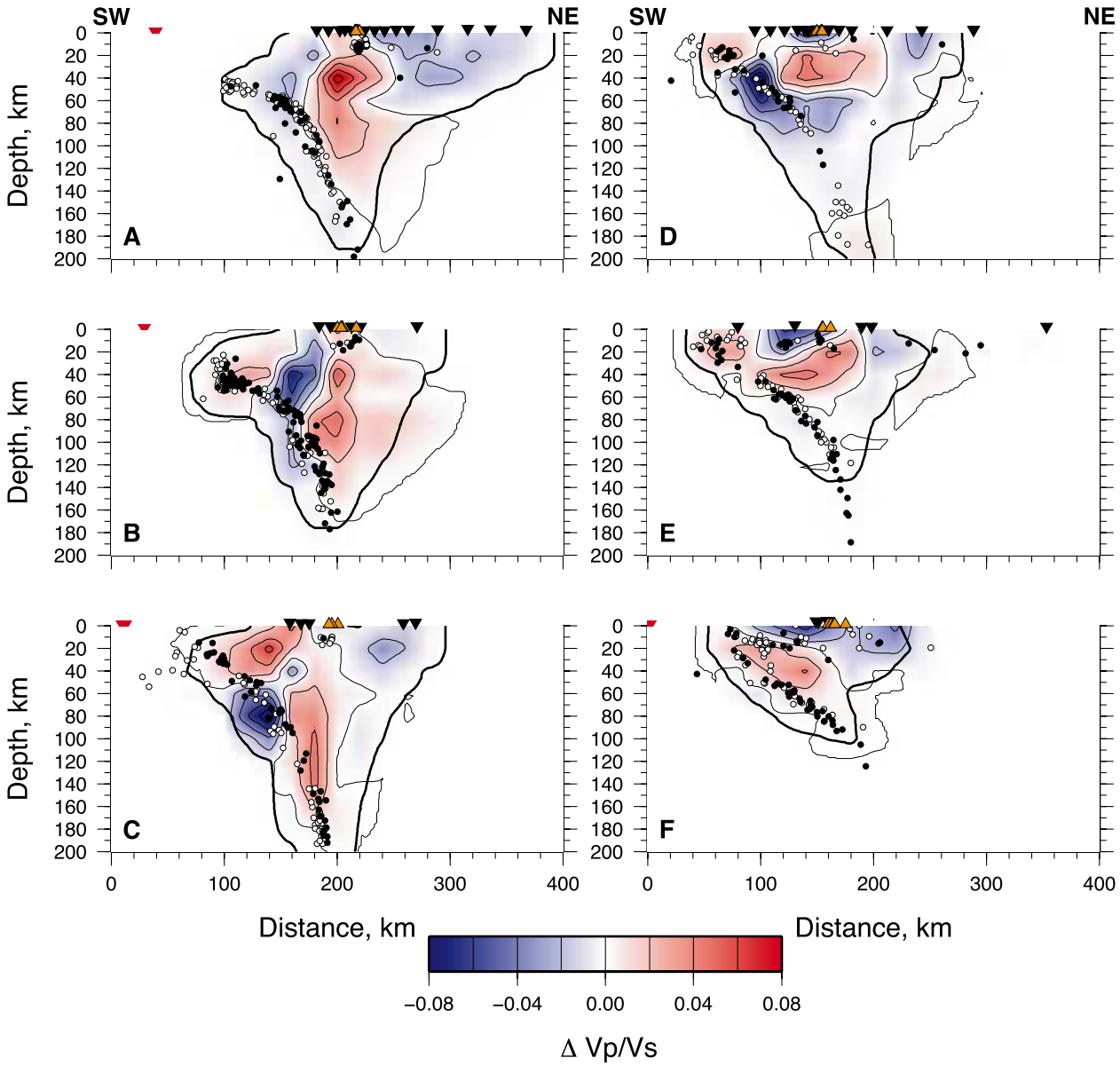

Figure 8. Cross sections through the final *Vp*/*Vs* model, shown as perturbations to the 1-D model (Figure 4). The model is shown for regions of the grid containing 10 or more rays, with resolutions contours and earthquake coloring the same as in Figure 7. See Figure 1 for the locations of cross sections. Symbols same as Figure 3.

defined as the region below a reference surface following the top of the WBZ. The observed slow *Vp* layer diminishes and velocities increase to their a priori values by 40 km beneath the reference surface, where ray coverage for paths within the slab becomes poor. The raypaths that sample the slab are diving trench-parallel along-strike paths, so tradeoffs might exist between the thickness of the slow layer and velocity gradients. Hence, the actual thickness of this slow layer may be biased by smoothing and ray sampling.

[37] To determine the minimum recoverable thickness of this slow layer, several resolution tests are completed. For each test, the upper layer of the slab is set to the initial 1-D reference model (black line, Figure 4), while the lower layer remains set to the initial 1-D slab model (gray line, Figure 4). The thickness of the upper layer is increased in 5 km increments from 10 km to 60 km relative to the upper surface of the slab defined by WBZ seismicity. The inversion follows that done with actual data, including the same raypaths and data errors, with noise added. From cross sections in Nicaragua

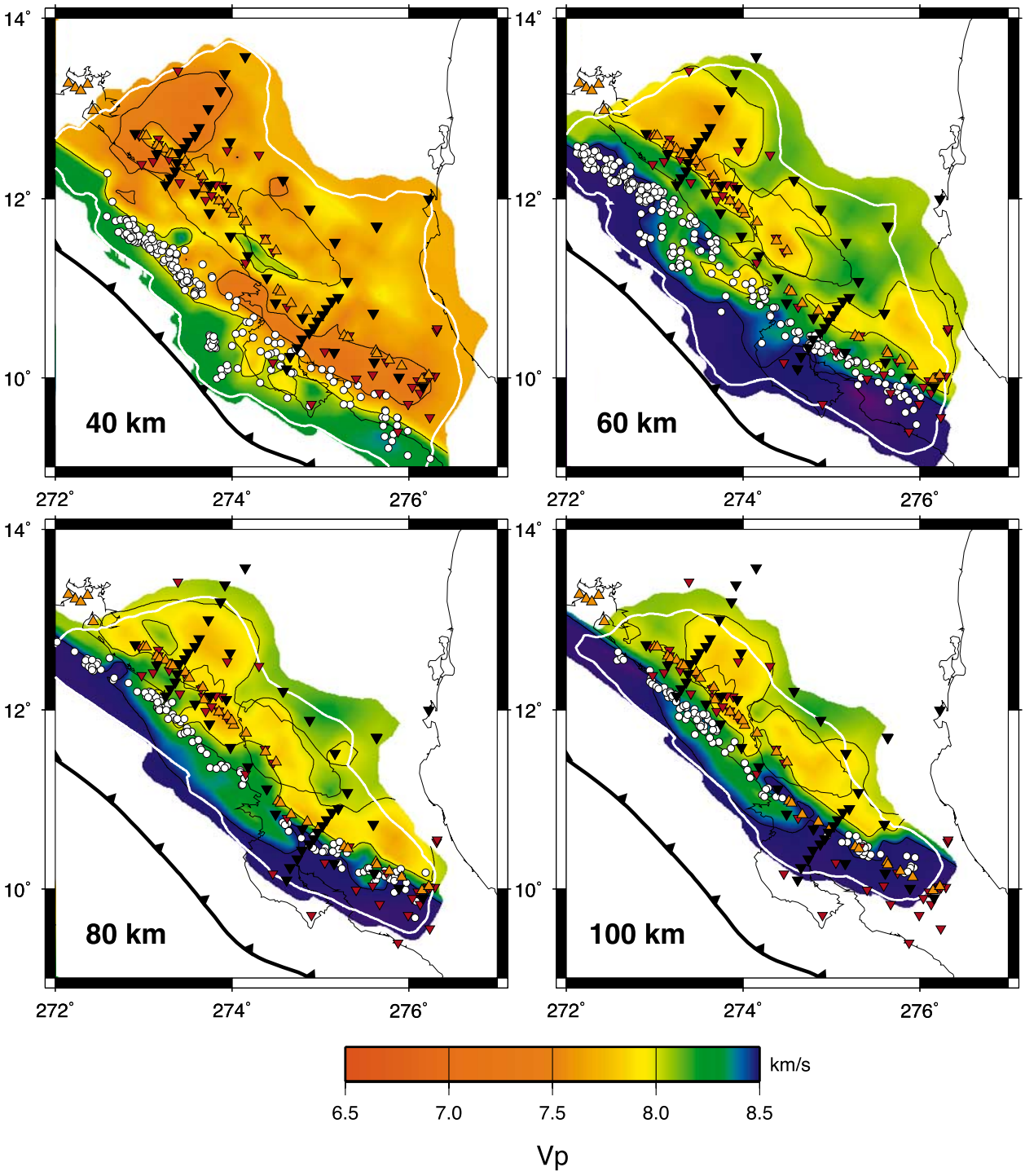

Figure 9. Maps of final *P* wave velocity model at various depths. Resolution limits the same as in Figure 7. White circles indicate earthquakes within 10 km of the depth slice. Note the presence of the reduced velocities within parts of the slab, and the broad region of reduced mantle velocities behind the volcanic front. Symbols same as Figure 1.

and Costa Rica, the recovered velocities are compared to the input model and to the actual final velocity model at 80 to 120 km depth by measuring the distance of the 8.5 km/s contour from the WBZ surface (Figure 13). The minimum layer thickness that gives results similar to those in the actual final velocity model is 35 to 40 km. For thicknesses larger than this, only the upper 35 to 40 km can be

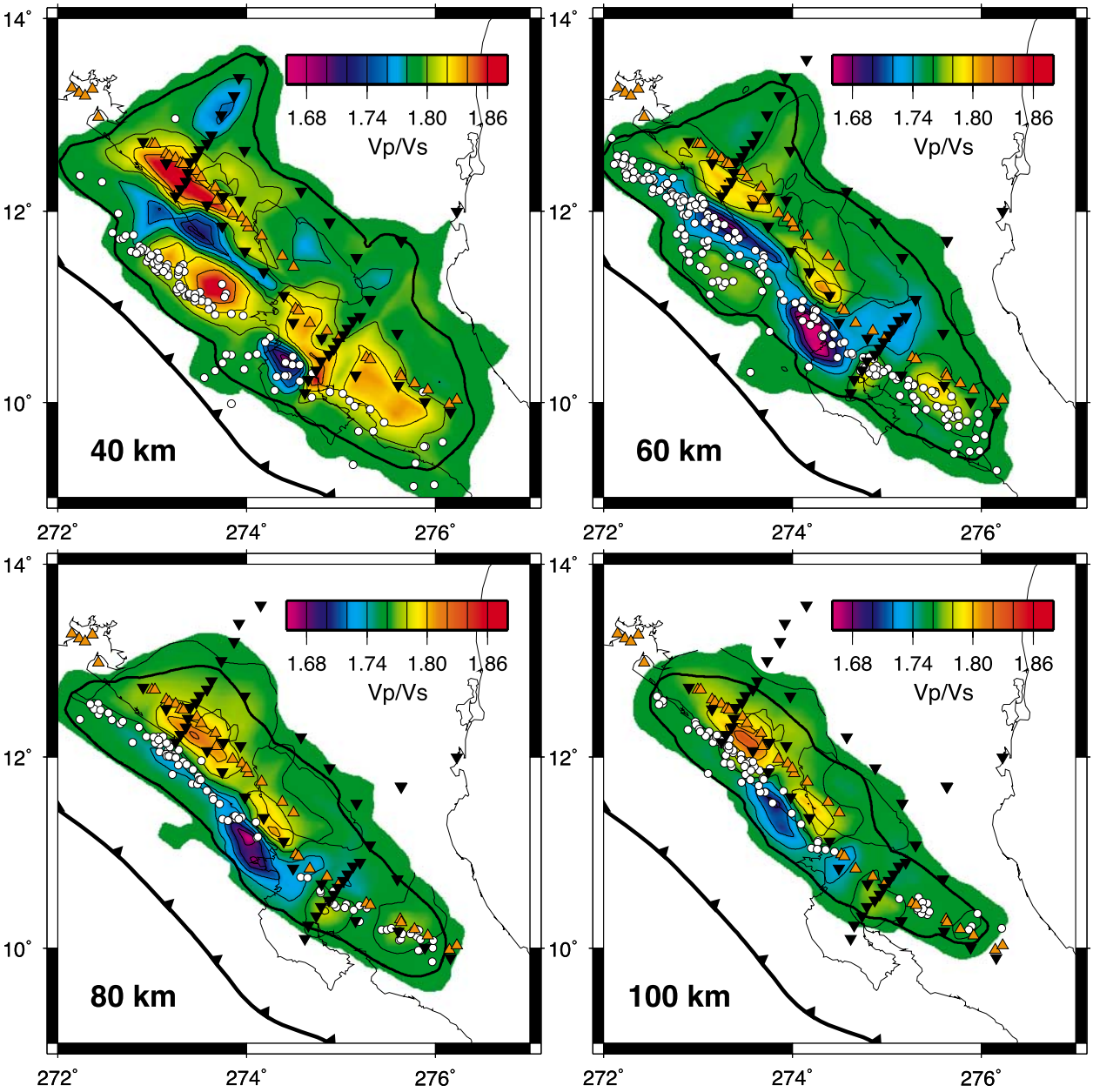

Figure 10. Maps of *Vp*/*Vs* model at various depths. Resolution limits the same as in Figure 7. White circles indicate earthquakes within 10 km of the depth slice. Note the continuous sheet of elevated *Vp*/*Vs* near the volcanic front beneath Nicaragua. Symbols same as Figure 1.

recovered. Beneath Costa Rica, recovery of a reduced velocity layer is similar, although no reduced slab velocities are observed in the actual data.

[38] However, these thicknesses are relative to a reference slab surface that lies at the top of the WBZ hypocenters, and to the extent that the WBZ is widened by hypocentral error, this slab surface may incorporate part of the overlying mantle wedge [*Syracuse and Abers*, 2006]. Figure 13 shows histograms of hypocentral distances below the surface measured normal to it. If all thickness of the Wadati-Benioff zone is due to errors in earthquake locations and all seismicity actually lies along a surface with zero thickness, the seismicity surface would lie on average 10 ± 1 km deeper than the digitized surface. Assuming that the seismicity lies at the center of a 7 km thick layer of oceanic crust and overlying sediments [*Ranero et al.*, 2003], the low-velocity layer in Nicaragua extends

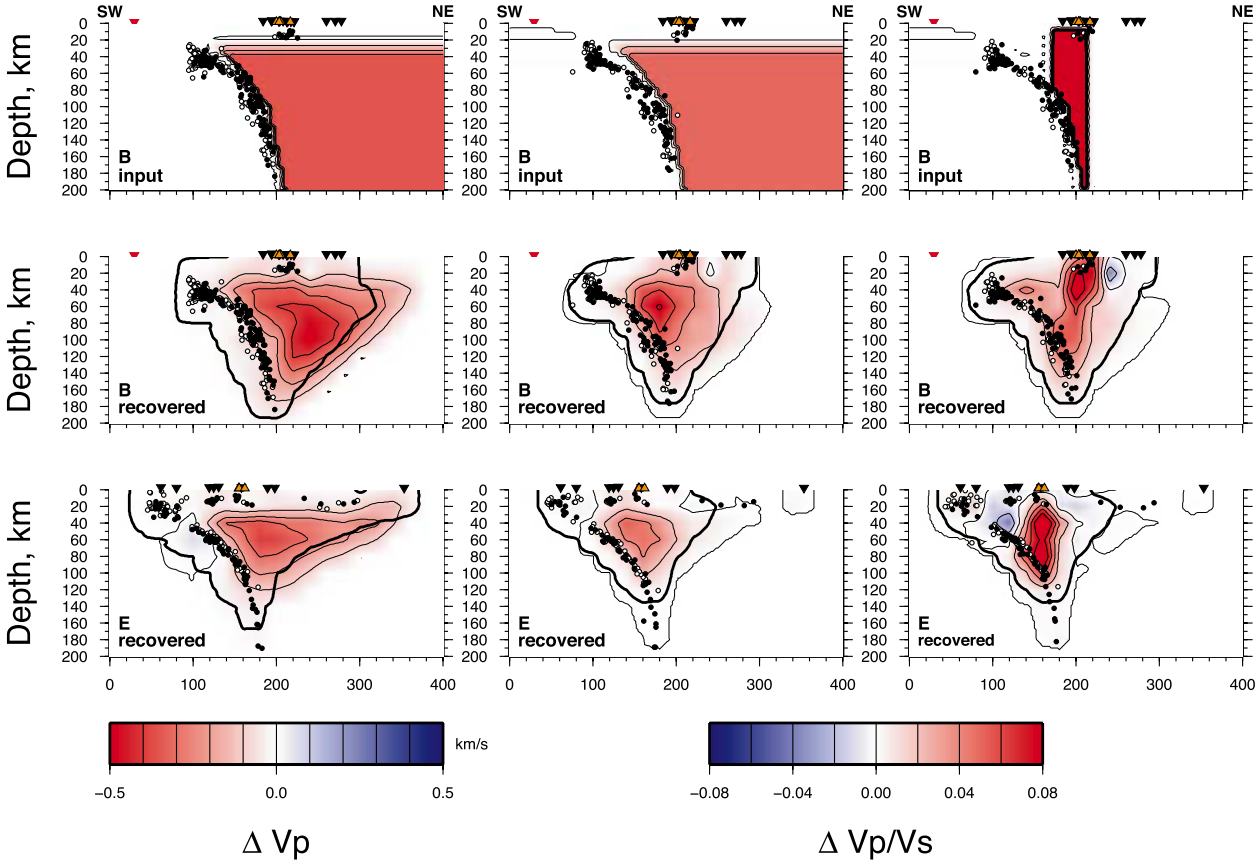

Figure 11. Resolution test for recovery of an input model with *Vp* reduced by 0.35 km/s (top left) and wedge *Vp*/*Vs* increased by 0.05, either for the entire wedge (top middle) or in the form of a 40 km wide sheet in the wedge (top right). Velocity perturbations follow the predictions for a 300°C increase in wedge temperature [*Faul and Jackson*, 2005]. See Figure 1 for the locations of cross sections. Resolution limits the same as in Figure 7. Symbols same as Figure 3.

20 to 28 km below the slab surface including crust and sediments, or 13 to 21 km into the mantle.

[39] These tests also indicate that there is equal or better recovery in Costa Rica compared to Nicaragua (Figures 12 and 13), showing that the absence of a slow layer within the Costa Rican slab is well constrained (Figures 7e, 7f, and 9). Even though ray density varies considerably along strike, the recovery for *Vp* is roughly constant throughout the imaged study area, and small variations in along-strike recovery of *Vp*/*Vs* do not correspond to any imaged structure that we interpret as a hydrated slab (Figure 12).

7. Discussion

7.1. Slab Geometry

[40] The lack of a break or contortion in the slab at the shift in the volcanic front at the Nicaragua/Costa Rica border (11°N) indicates that the shift cannot be caused by changes in slab geometry, as was previously hypothesized [*Carr and Stoiber*, 1977]. The shift in the volcanic front must be caused by differences in the location of melting within the mantle wedge, or by differences in melt flow paths within the crust of the upper plate. The *Vp*/*Vs* anomalies reflect melt distribution and provide some insight.

7.2. Wedge Temperature and Melt Distribution

[41] The effects of temperature on seismic velocities are reasonably understood. Taking into account both anharmonic and anelastic effects on *P* wave velocities, mantle velocities of 7.6–8.2 km/s beneath the Nicaraguan volcanic front and back arc are consistent with dry olivine temperatures in the range of 1050–1500°C, based on calibrations of *Faul and Jackson* [2005] and assuming a grain size between 1 mm and 10 mm and a frequency of 5 Hz.

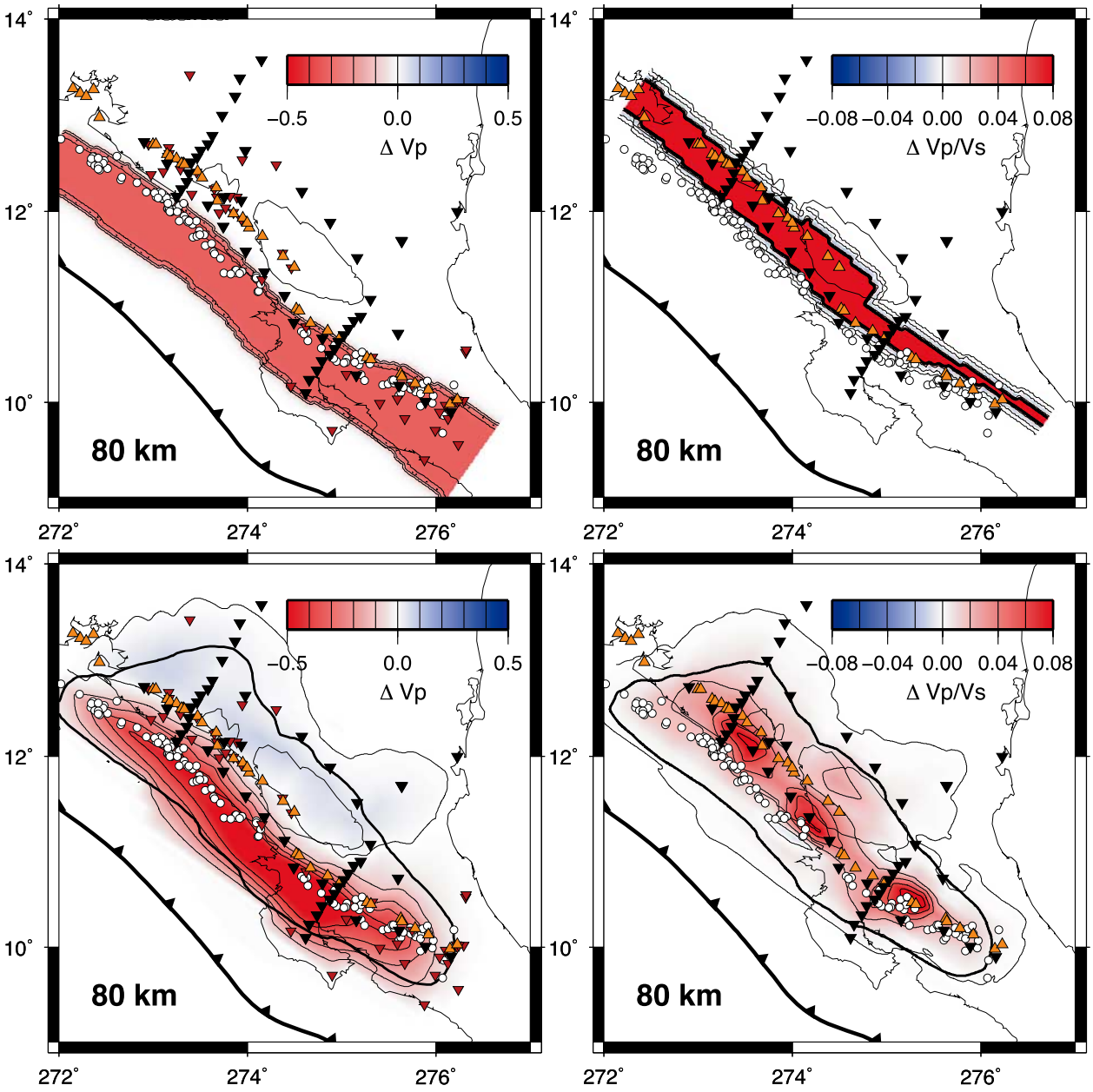

Figure 12. Resolution tests for recovery of a reduced velocity layer in the slab and a high *Vp*/*Vs* sheet in the wedge, shown in map view at 80 km depth. The input to the *Vp* test (top left) has starting slab velocities set to initial mantle wedge velocities for 50 km below the slab surface. The *Vp*/*Vs* test is the same as the 40 km wide sheet in Figure 11. The recovered velocities are shown in the bottom two panels below the respective input models. Resolution limits the same as in Figure 7. Symbols same as Figure 1.

The presence of water or melt lowers the temperature estimates, as do decreases in grain size. Mantle velocities beneath the Costa Rican volcanic front and back arc are on average slightly higher, however due to poorer resolution beneath Costa Rica than beneath Nicaragua, this difference may not reflect any difference in wedge temperatures. The highest of these temperatures [*Hirschmann*, 2000] exceed the dry solidus, so water or melt are probably present.

[42] In the "cold nose" of the wedge corner where *P* wave velocities are 7.1–8.0 km/s, velocities may be reduced despite cold temperatures (Rychert et al., submitted manuscript, 2008) by the presence of serpentine. The presence of serpentine in the

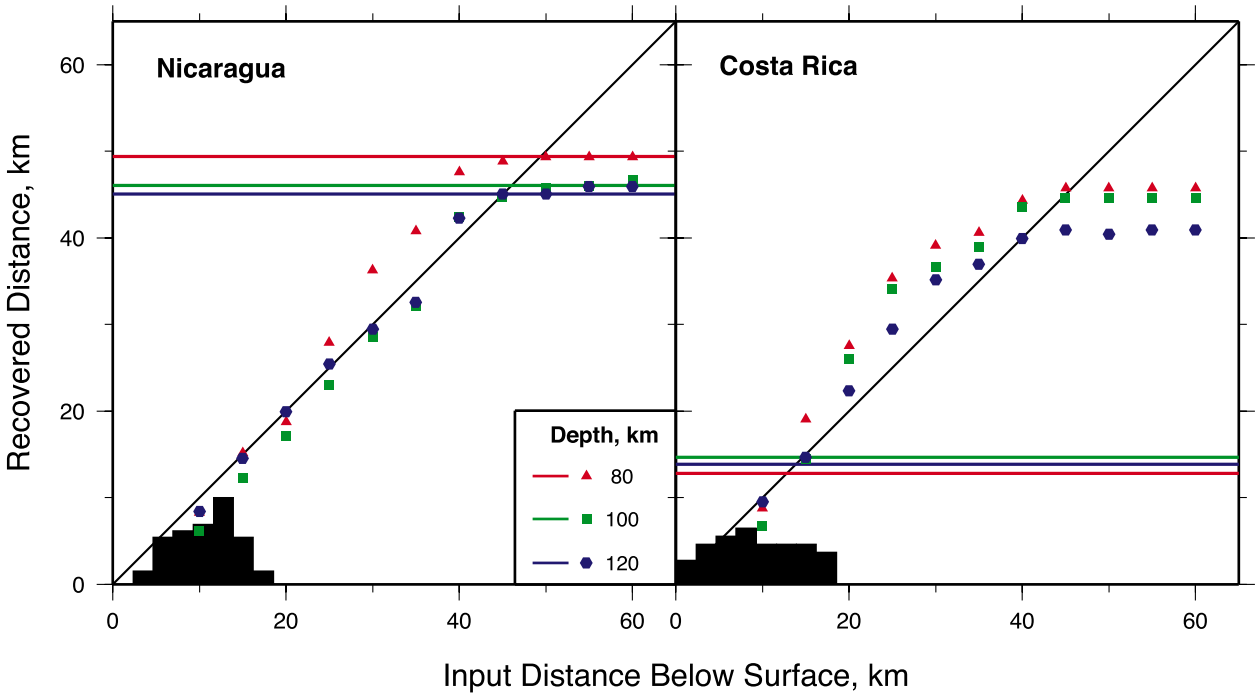

Figure 13. Resolution test for recovery of a reduced velocity layer in the upper portion of the slab beneath Nicaragua and Costa Rica. Points indicate the distance below the digitized slab surface where velocities of 8.5 km/s are recorded in the input and recovered models. For each input model, the starting slab velocities are set to initial mantle wedge velocities for a specified distance below the slab surface. Horizontal lines indicate the distance from the slab surface at which the velocity in the actual tomographic model is 8.5 km/s. Histograms show the distribution of earthquakes beneath the slab surface. If the actual slab surface lies at the center of seismicity, then the slab surface derived using the top of seismicity is biased ~10 km into the overlying mantle. For example, for an input distance of 20 km, the slab is drawn 10 km too shallow based on the center of seismicity, and the input model therefore only has reduced velocities 10 km into the actual slab.

wedge corner may cause the weakening of the observed Moho signal in the fore arc, as seen in receiver functions [*DeShon and Schwartz*, 2004; *MacKenzie et al.*, 2008]. A consistent analysis incorporating attenuation (Rychert et al., submitted manuscript, 2008) and velocities will provide clearer temperature and fluid constraints for the mantle wedge.

[43] If the region of elevated *Vp*/*Vs* that is observed beneath the arc in Nicaragua were due to temperature alone it should have the same geometry as the low *Vp* region of the mantle wedge. By plotting *Vp* versus *Vp*/*Vs* for individual nodes in the Nicaraguan mantle wedge, two distinct trends emerge (Figure 14). One follows a trend similar to that of increasing temperature, following *Karato* [1993] and assuming a Q of ∞, for a high-frequency signal in which anelastic effects are negligible. The second contains points within the high *Vp*/*Vs* sheet and follows a trend similar to that obtained by decreasing shear modulus alone, for constant bulk modulus. Melting of a small fraction of mantle could provide this effect through a number of mechanisms [*Takei*, 2002; *Faul et al.*, 2004].

[44] The effects of melt on *Vp*/*Vs* remain poorly understood. From tests of olivine samples done with similar grain sizes, temperatures, and frequencies, *Gribb and Cooper* [2000] find that 5 wt. % melt reduces Q_s by a maximum of an order of magnitude, whereas *Faul et al.* [2004] find that only 1 vol. % melt has similar results. The resulting drop in *Vs* through anelastic dispersion would vary similarly [*Karato*, 1993]. *Takei* [2002] and *Hammond and Humphreys* [2000] investigate poro-elastic effects and find that melt decreases *Vs* more than it decreases *Vp* due to a decrease in shear modulus, but not bulk modulus, leading to an increase in *Vp*/*Vs* as *Vp* decreases, particularly as melt fractions increase above 1%. Pore geometry also affects the magnitudes of changes in velocity [*Hammond and Humphreys*, 2000; *Takei*, 2002]. These uncertainties, in addition to imperfect *Vp*/*Vs*

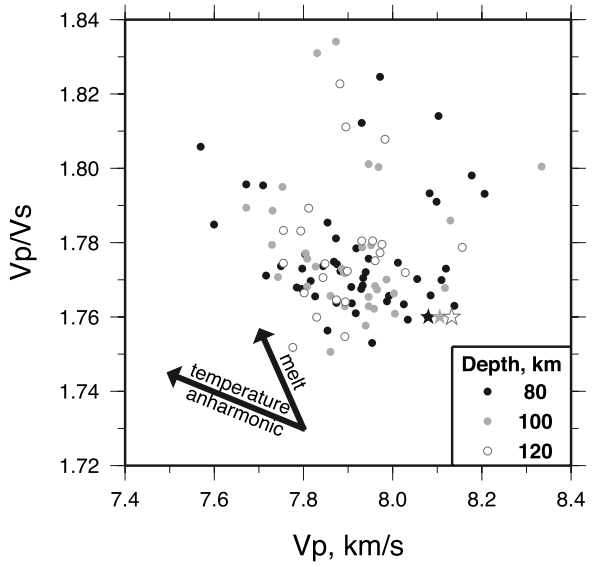

Figure 14. *Vp* versus *Vp*/*Vs* for the Nicaraguan mantle wedge for parts of the model with 50 or more rays. Stars represent the starting *Vp* and *Vp*/*Vs* values for each depth. Arrows indicate the slope along a path of increasing temperature [*Karato*, 1993] and the slope along a path of decreasing shear modulus, such as might occur when increasing melt fraction [*Hammond and Humphreys*, 2000].

anomaly amplitude resolution, make it difficult to quantify the amount of melt that would be necessary to cause the observed sheet of high *Vp*/*Vs*. Given its location, however, it seems plausible that it is due to melt, generated near the slab and ascending nearly vertically to the arc. Similar geometry is seen in numerical models of wet melting beneath arcs [*Cagnioncle et al.*, 2007]. By contrast, a tomographic image of Honshu [*Nakajima et al.*, 2001] shows a dipping region of low *Vp* along the top of the slab, interpreted to be melt rising to the arc. The difference between the shape of the observed melting regions in Honshu and Nicaragua may be due to the comparatively steeper slab dip and higher water flux beneath Nicaragua. The offset of 30 km from the volcanic front seen in southern Nicaragua (Figure 10) may be caused by focusing of melt in the upper plate or just below the Moho by upper plate structure [*MacKenzie et al.*, 2008].

7.3. Slab and Serpentinization

[45] The reduced *P* wave velocities (4 to 6% below the starting *Vp*) in the upper part of the slab beneath Nicaragua are potentially caused by hydration of the crust and upper mantle of the slab, proposed to be initiated at the outer rise near the trench [*Rüpke et al.*, 2002; *Ranero et al.*, 2003]. Previously, a ~15% reduced velocity waveguide at the top of the subducting plate that is 2.5–6 km thick has been found [*Abers et al.*, 2003], but the reduced velocities here extend over a region at least 20 km thick. Serpentinization of mantle lithosphere could produce these results. If these reduced mantle velocities are caused by serpentinization, approximately 10–20 wt. % serpentine would be necessary to explain the velocity reduction of 4 to 6% seen beneath Nicaragua [*Hacker and Abers*, 2004]. This is consistent with the findings from a refraction study of the Cocos plate near the trench at this latitude that show upper mantle (*Pn*) velocities ~5% lower than typical of the Cocos plate corresponding to 12–17% serpentinization [*Ivandic et al.*, 2008]. Thus, all of the serpentinized subducting plate survives to 150 km depth, as predicted from thermal and petrological considerations [*Peacock et al.*, 2005]. The presence of a serpentinized mantle layer beneath Nicaragua and not beneath Costa Rica correlates with geochemical studies indicating unusual oxygen isotope ratios in Nicaraguan magmas that suggest a serpentine source for fluids there [*Eiler et al.*, 2005] and generally greater water in Nicaraguan arc magmas than in Costa Rican ones [*Wade et al.*, 2006].

[46] Regions of reduced *Vp*/*Vs* (1.68 to 1.74) within and beneath the Wadati-Benioff zone may also indicate the presence of free water. Pore spaces may not be interconnected enough to allow water to move rapidly out of the slab and into the mantle wedge [*Watson and Lupulescu*, 1993], trapping some free water within the slab. Disconnected pores of compressible fluid provide a geometry that could lead to low *Vp*/*Vs* [*Takei*, 2002].

7.4. Double Seismic Zones

[47] Double seismic zones have been detected in several subduction zones, but it is unclear whether these are rare features [i.e., *Kao and Chen*, 1994] or common [*Brudzinski et al.*, 2007]. *Brudzinski et al.* [2007] find evidence of double seismic zones between 70 and 150 km depth in almost all subduction zones with spacing that correlated with plate age, including a section of the Cocos plate immediately to the north of the TUCAN array. For a slab age of roughly 20 Ma, *Brudzinski et al.* [2007] predict a double seismic zone separation of 3–11 km. To investigate the possibility of a double seismic zone beneath Nicaragua and Costa Rica, a line is fitted to earthquakes between 70 and 150 km

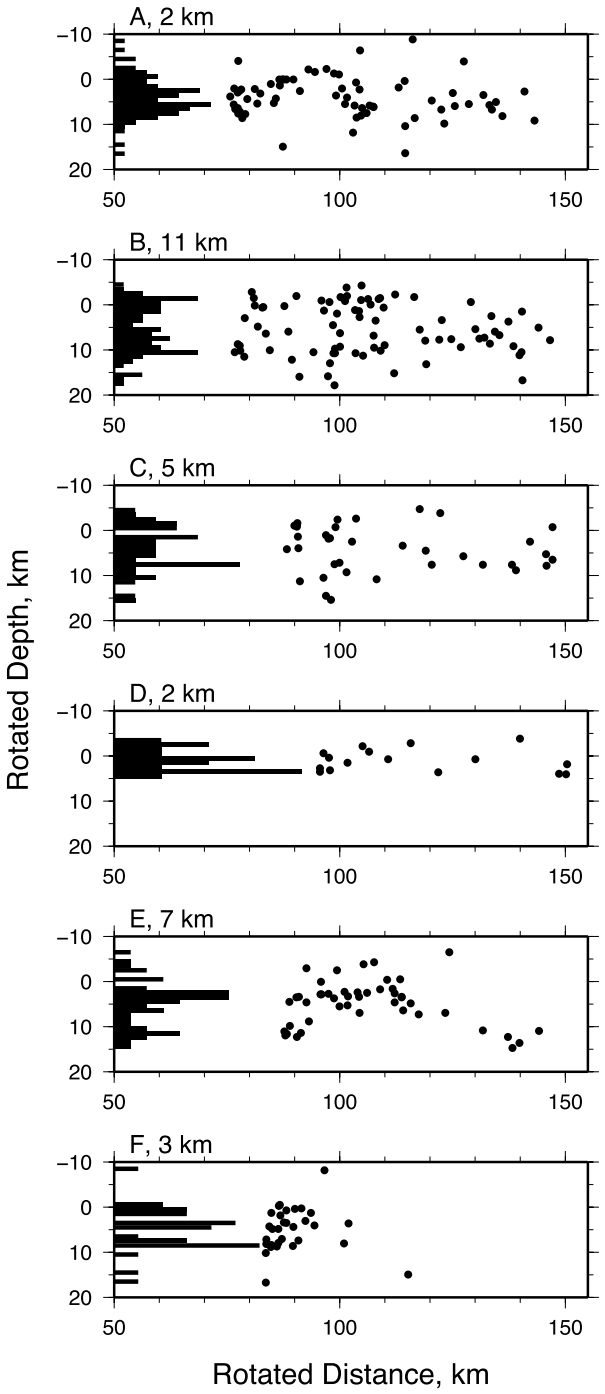

Figure 15. Histograms and plots of earthquakes rotated into downdip and slab-normal coordinates for earthquakes between 70 km and 150 km depth, following *Brudzinski et al.* [2007]. Each panel contains earthquakes within 40 km along strike of the given cross section. Histograms are shown as relative percentages of earthquakes, and layer separation is calculated as the distance between the two largest peaks in the histogram. Note the strong bimodal distribution for cross section B.

depth within each cross section and the distance from this line to each earthquake is calculated and plotted (Figure 15) in the manner of *Brudzinski et al.* [2007]. Histograms of earthquake distance to the best fit line show a bimodal distribution for cross section B with a layer separation of 11 km fitted by eye. Other cross sections show weaker bimodal distributions with smaller layer separations, ranging from 2 to 7 km (Figure 15), and all seismicity could occur within the 7 km thick subducting crust [*Hacker et al.*, 2003]. Thus, a double seismic zone is present in one region but not clearly in others. This is similar to the variability seen in the eastern Aleutians [*Hudnut and Taber*, 1987].

[48] A possible cause of the lower layer of seismicity within double seismic zones is dehydration embrittlement after water is released from serpentinized mantle [*Peacock*, 1991; *Kirby et al.*, 1996]. Here, the region in which a double seismic zone is most likely is also the region of strongest slab serpentinization. However, the region of apparent slab serpentinization extends over a broader area, so some other condition must be necessary for lower zone seismicity.

8. Conclusions

[49] The tomographic results and hypocenter relocations from the TUCAN experiment have illuminated the structure of the slab beneath Nicaragua and Costa Rica. Hypocenters indicate a Wadati-Benioff zone that is less than 20 km thick and less than 15 km thick in most places. All seismicity could be inside subducted crust, given hypocentral uncertainties, consistent with inferences made from guided-wave studies [*Abers*, 2005]. The slab dips 50–60° beneath most of Nicaragua and Costa Rica, with no resolvable change in slab geometry where the arc shifts 40 km at the Nicaragua-Costa Rica border, although slab dip does decrease at the southeastern end of the array in central Costa Rica.

[50] The tomographic results have imaged the cycle of water from subduction to release into the wedge and initiation of melting, and link observations of hydration at the trench to arc output. Seismic velocities in the subducting crust and upper mantle of the Cocos plate are lower than predicted beneath Nicaragua at 60–140 km depth, indicating 10–20 wt. % serpentinization extending 20 to 28 km beneath the surface of the slab. The reduced velocities are not present in the slab

beneath Costa Rica, probably reflecting lower volatile transport by the slab and ultimately to the mantle wedge. This change in slab hydration may explain lower volatile and geochemical tracer outputs from Costa Rican volcanoes than from Nicaraguan volcanoes.

[51] Within the mantle wedge, reduced *P* wave velocities indicate temperatures of 1050–1500°C beneath Nicaragua, based on dry, melt-free conditions, with temperatures or water contents beneath Costa Rica possibly lower than Nicaragua. A sheet of high *Vp*/*Vs* ratios beneath the volcanic front in Nicaragua may be a sheet of melt, whereas high *Vp/Vs* ratios beneath Costa Rica are broader and weaker, caused by a less defined melt region. Overall, Nicaragua can be characterized by a hydrated slab, a hot wedge, and a well-defined region of melt beneath the volcanoes, and Costa Rica can be characterized by less pervasive hydration throughout the slab and wedge, a possibly slightly cooler wedge, and a broader, less concentrated region of melt.

[52] Further seismic investigation of portions of other subduction zones where there are large variations in the location of the volcanic front over short distances, would help improve the understanding of what causes these changes in the location of magmatism. Are they all associated with changes in the location of the hottest part of the mantle wedge and varying upper plate structure? Tomography of subduction zones where volcanoes have high water contents would also assist in resolving whether subducted mantle serpentinization is a unique feature to Nicaragua, or is a common feature of many subduction zones.

Acknowledgments

[53] We thank the large group who made the TUCAN data collection possible: P. Peres and A. Morales and many others at INETER, J. Pacheco at OVSICORI, T. Parker, N. Barstow, and others from the PASSCAL Instrument Center, D. Abt, A. Walker, and M. Salas at Brown University, and G. Reyes at Boston University. S. Roecker and A. Ferris provided codes and assistance with early stages of the analysis. This work benefited from discussions with numerous participants at the 2007 MARGINS-SFB574 Central America workshop and the thoughtful comments from D. Zhao, an anonymous reviewer, and editor V. Salters. This work is supported by National Science Foundation grant OCE-0203650.

References

Abers, G. A. (2005), Seismic low-velocity layer at the top of subducting slabs: Observations, predictions, and systematics, *Phys. Earth Planet Inter.*, *149*(1–2), 7–29, doi:10.1016/j.pepi.2004.10.002.

Abers, G. A., T. Plank, and B. R. Hacker (2003), The wet Nicaraguan slab, *Geophys. Res. Lett.*, *30*(2), 1098, doi:10.1029/2002GL015649.

Abt, D. L., K. M. Fischer, L. Martin, G. A. Abers, J. M. Protti, V. Gonzalez, and W. Strauch (2006), Shear-wave splitting tomography in the Central American subduction zone: Implications for flow and melt in the mantle wedge, *Eos Trans. AGU*, *87*(52), Fall Meet. Suppl., Abstract T22C-05.

Brudzinski, M. R., C. H. Thurber, B. R. Hacker, and E. R. Engdahl (2007), Global prevalence of double Benioff zones, *Science*, *316*(5830), 1472–1474, doi:10.1126/science.1139204.

Cagnioncle, A.-M., E. M. Parmentier, and L. T. Elkins-Tanton (2007), Effect of solid flow above a subducting slab on water distribution and melting at convergent plate boundaries, *J. Geophys. Res.*, *112*, B09402, doi:10.1029/2007JB004934.

Carr, M. J., and R. J. Stoiber (1977), Geologic setting of some destructive earthquakes in Central America, *Geol. Soc. Am. Bull.*, *88*, 151–156, doi:10.1130/0016-7606(1977)88<151:GSOSDE>2.0.CO;2.

Christensen, N. I. (1996), Poisson's ratio and crustal seismology, *J. Geophys. Res.*, *101*(B2), 3139–3156, doi:10.1029/95JB03446.

Colombo, D., G. B. Cimini, and R. deFranco (1997), Three-dimensional velocity structure of the upper mantle beneath Costa Rica from a teleseismic tomography study, *Geophys. J. Int.*, *131*(2), 189–208, doi:10.1111/j.1365-246X.1997.tb01216.x.

Conder, J. A., and D. A. Wiens (2006), Seismic structure beneath the Tonga arc and Lau back-arc basin determined from joint Vp, Vp/Vs tomography, *Geochem. Geophys. Geosyst.*, *7*, Q03018, doi:10.1029/2005GC001113.

Davies, J. H., and D. J. Stevenson (1992), Physical model of source region of subduction zone volcanics, *J. Geophys. Res.*, *97*(B2), 2037–2070, doi:10.1029/91JB02571.

DeShon, H. R., and S. Y. Schwartz (2004), Evidence for serpentinization of the forearc mantle wedge along the Nicoya Peninsula, Costa Rica, *Geophys. Res. Lett.*, *31*, L21611, doi:10.1029/2004GL021179.

DeShon, H. R., S. Y. Schwartz, A. V. Newman, V. Gonzalez, M. Protti, L. R. M. Dorman, T. H. Dixon, D. E. Sampson, and E. R. Flueh (2006), Seismogenic zone structure beneath the Nicoya Peninsula, Costa Rica, from three-dimensional local earthquake P- and S-wave tomography, *Geophys. J. Int.*, *164*(1), 109–124, doi:10.1111/j.1365-246X.2005.02809.x.

Dziewonski, A. M., T.-A. Chou, and J. H. Woodhouse (1981), Determination of earthquake source parameters from waveform data for studies of global and regional seismicity, *J. Geophys. Res.*, *86*, 2825–2852, doi:10.1029/JB086iB04p02825.

Eiler, J. M., M. J. Carr, M. Reagan, and E. Stolper (2005), Oxygen isotope constraints on the sources of Central American arc lavas, *Geochem. Geophys. Geosyst.*, *6*, Q07007, doi:10.1029/2004GC000804.

Engdahl, E. R., R. van der Hilst, and R. Buland (1998), Global teleseismic earthquake relocation with improved travel times and procedures for depth determination, *Bull. Seismol. Soc. Am.*, *88*(3), 722–743.

England, P., and C. Wilkins (2004), A simple analytical approximation to the temperature structure in subduction zones, *Geophys. J. Int.*, *159*(3), 1138–1154, doi:10.1111/j.1365-246X.2004.02419.x.

England, P., R. Engdahl, and W. Thatcher (2004), Systematic variation in the depths of slabs beneath arc volcanoes,

Geophys. J. Int., *156*(2), 377–408, doi:10.1111/j.1365-246X.2003.02132.x.

Faul, U. H., and I. Jackson (2005), The seismological signature of temperature and grain size variations in the upper mantle, *Earth Planet. Sci. Lett.*, *234*(1–2), 119–134, doi:10.1016/j.epsl.2005.02.008.

Faul, U. H., J. D. Fitz Gerald, and I. Jackson (2004), Shear wave attenuation and dispersion in melt-bearing olivine polycrystals: 2. Microstructural interpretation and seismological implications, *J. Geophys. Res.*, *109*, B06202, doi:10.1029/2003JB002407.

Gorbatov, A., J. Dominguez, G. Suarez, V. Kostoglodov, D. Zhao, and E. Gordeev (1999), Tomographic imaging of the P wave velocity structure beneath the Kamchatka peninsula, *Geophys. J. Int.*, *137*(2), 269–279, doi:10.1046/j.1365-246X.1999.00801.x.

Gribb, T. T., and R. F. Cooper (2000), The effect of an equilibrated melt phase on the shear creep and attenuation behavior of polycrystalline olivine, *Geophys. Res. Lett.*, *27*(15), 2341–2344, doi:10.1029/2000GL011443.

Hacker, B. R., and G. A. Abers (2004), Subduction Factory: 3. An Excel worksheet and macro for calculating the densities, seismic wave speeds, and H_2O contents of minerals and rocks at pressure and temperature, *Geochem. Geophys. Geosyst.*, *5*, Q01005, doi:10.1029/2003GC000614.

Hacker, B. R., S. M. Peacock, G. A. Abers, and S. D. Holloway (2003), Subduction factory: 2. Are intermediate-depth earthquakes in subducting slabs linked to metamorphic dehydration reactions?, *J. Geophys. Res.*, *108*(B1), 2030, doi:10.1029/2001JB001129.

Hammond, W. C., and E. D. Humphreys (2000), Upper mantle seismic wave velocity: Effects of realistic partial melt geometries, *J. Geophys. Res.*, *105*(B5), 10,975–10,986, doi:10.1029/2000JB900041.

Hirschmann, M. M. (2000), Mantle solidus: Experimental constraints and the effects of peridotite composition, *Geochem. Geophys. Geosyst.*, *1*(10), 1042, doi:10.1029/2000GC000070.

Hole, J. A., and B. C. Zelt (1995), 3-D finite-difference reflection travel-times, *Geophys. J. Int.*, *121*(2), 427–434, doi:10.1111/j.1365-246X.1995.tb05723.x.

Hudnut, K. W., and J. J. Taber (1987), Transition from double to single Wadati-Benioff seismic zone in the Shumagin Islands, Alaska, *Geophys. Res. Lett.*, *14*(2), 143–146, doi:10.1029/GL014i002p00143.

Husen, S., R. Quintero, E. Kissling, and B. Hacker (2003), Subduction-zone structure and magmatic processes beneath Costa Rica constrained by local earthquake tomography and petrological modelling, *Geophys. J. Int.*, *155*(1), 11–32, doi:10.1046/j.1365-246X.2003.01984.x.

Hyndman, R. D., and S. M. Peacock (2003), Serpentinization of the forearc mantle, *Earth Planet. Sci. Lett.*, *212*(3–4), 417–432, doi:10.1016/S0012-821X(03)00263-2.

Ivandic, M., I. Grevemeyer, A. Berhorst, E. R. Flueh, and K. McIntosh (2008), Impact of bending related faulting on the seismic properties of the incoming oceanic plate offshore of Nicaragua, *J. Geophys. Res.*, B05410, doi:10.1029/2007JB005291.

Kao, H., and W. P. Chen (1994), The double seismic zone in Kuril-Kamchatka: The tale of 2 overlapping single zones, *J. Geophys. Res.*, *99*(B4), 6913–6930, doi:10.1029/93JB03409.

Kárason, H., and R. D. van der Hilst (2001), Tomographic imaging of the lowermost mantle with differential times of refracted and diffracted core phases (PKP, P-diff), *J. Geophys. Res.*, *106*(B4), 6569–6587, doi:10.1029/2000JB900380.

Karato, S. (1993), Importance of anelasticity in the interpretation of seismic tomography, *Geophys. Res. Lett.*, *20*(15), 1623–1626, doi:10.1029/93GL01767.

Karato, S. I. (2003), Mapping water content in the upper mantle, in *Inside the Subduction Factory*, *Geophys. Monogr. Ser.*, vol. 138, edited by J. Eiler, pp. 135–152, AGU, Washington, D. C.

Kirby, S. H., S. Stein, E. A. Okal, and D. C. Rubie (1996), Metastable mantle phase transformations and deep earthquakes in subducting oceanic lithosphere, *Rev. Geophys.*, *34*(2), 261–306, doi:10.1029/96RG01050.

Lay, T. (1997), *Structure and Fate of Subducting Slabs*, 185 pp., Academic, San Diego, Calif.

MacKenzie, L., G. A. Abers, K. M. Fischer, E. M. Syracuse, J. M. Protti, V. Gonzalez, and W. Strauch (2008), Crustal structure along the southern Central American volcanic front, *Geochem. Geophys. Geosyst.*, doi:10.1029/2008GC001991, in press.

Matumoto, T., M. Ohtake, G. Latham, and J. Umana (1977), Crustal structure in southern Central America, *Bull. Seismol. Soc. Am.*, *67*(1), 121–134.

McLaren, J. P., and C. Frohlich (1985), Model calculations of regional network locations for earthquakes in subduction zones, *Bull. Seismol. Soc. Am.*, *75*(2), 397–413.

Menke, W. (1984), *Geophysical Data Analysis: Discrete Inverse Theory*, 260 pp., Academic, Orlando, Fla.

Morris, J. D., W. P. Leeman, and F. Tera (1990), The subducted component in island-arc lavas—Constraints from Be isotopes and B-Be systematics, *Nature*, *344*(6261), 31–36, doi:10.1038/344031a0.

Mueller, G. (1971), Approximate treatment of elastic body waves in media with spherical symmetry, *Geophys. J. R. Astron. Soc.*, *23*(4), 435–449.

Nakajima, J., T. Matsuzawa, A. Hasegawa, and D. Zhao (2001), Three-dimensional structure of V_p, V_s, and V_p/V_s beneath northeastern Japan: Implications for arc magmatism and fluids, *J. Geophys. Res.*, *106*(B10), 21,843–21,857, doi:10.1029/2000JB000008.

Paige, C. C., and M. A. Saunders (1982), LSQR: An algorithm for sparse linear equations and sparse least squares, *Trans. Math. Software*, *8*(1), 43–71, doi:10.1145/355984.355989.

Patino, L. C., M. J. Carr, and M. D. Feigenson (2000), Local and regional variations in Central American arc lavas controlled by variations in subducted sediment input, *Contrib. Mineral. Petrol.*, *138*(3), 265–283, doi:10.1007/s004100050562.

Peacock, S. M. (1991), Numerical simulation of subduction zone pressure temperature time paths—Constraints on fluid production and arc magmatism, *Philos. Trans. R. Soc. London, Ser. A*, *335*(1638), 341–353, doi:10.1098/rsta.1991.0050.

Peacock, S. M., P. E. van Keken, S. D. Holloway, B. R. Hacker, G. A. Abers, and R. L. Fergason (2005), Thermal structure of the Costa Rica - Nicaragua subduction zone, *Phys Earth Planet Inter*, *149*(1–2), 187–200, doi:10.1016/j.pepi.2004.08.030.

Pisarenko, V. F., A. F. Kushnir, and I. V. Savin (1987), Statistical adaptive algorithms for estimation of onset moments of seismic phases, *Phys Earth Planet Inter*, *47*, 4–10, doi:10.1016/0031-9201(87)90062-8.

Plank, T., and C. H. Langmuir (1988), An evaluation of the global variations in the major element chemistry of arc basalts, *Earth Planet. Sci. Lett.*, *90*(4), 349–370, doi:10.1016/0012-821X(88)90135-5.

Plank, T., and C. H. Langmuir (1993), Tracing trace elements from sediment input to volcanic output at subduction zones, *Nature*, *362*(6422), 739–743, doi:10.1038/362739a0.

Protti, M., F. Gundel, and K. McNally (1994), The geometry of the Wadati-Benioff Zone under southern Central America and its tectonic significance—Results from a high-resolution local seismographic network, *Phys. Earth Planet Inter.*, *84*(1–4), 271–287, doi:10.1016/0031-9201(94)90046-9.

Protti, M., S. Y. Schwartz, and G. Zandt (1996), Simultaneous inversion for earthquake location and velocity structure beneath central Costa Rica, *Bull. Seismol. Soc. Am.*, *86*(1), 19–31.

Ranero, C. R., J. P. Morgan, K. McIntosh, and C. Reichert (2003), Bending-related faulting and mantle serpentinization at the Middle America trench, *Nature*, *425*(6956), 367–373, doi:10.1038/nature01961.

Reyners, M., D. Eberhart-Phillips, G. Stuart, and Y. Nishimura (2006), Imaging subduction from the trench to 300 km depth beneath the central North Island, New Zealand, with Vp and Vp/Vs, *Geophys. J. Int.*, *165*(2), 565–583, doi:10.1111/j.1365-246X.2006.02897.x.

Roecker, S., C. Thurber, K. Roberts, and L. Powell (2006), Refining the image of the San Andreas Fault near Parkfield, California using a finite difference travel time computation technique, *Tectonophysics*, *426*(1–2), 189–205, doi:10.1016/j.tecto.2006.02.026.

Rogers, R. D., H. Karason, and R. D. van der Hilst (2002), Epeirogenic uplift above a detached slab in northern Central America, *Geology*, *30*(11), 1031–1034, doi:10.1130/0091-7613(2002)030<1031:EUAADS>2.0.CO;2.

Rüpke, L. H., J. P. Morgan, M. Hort, and J. A. D. Connolly (2002), Are the regional variations in Central American arc lavas due to differing basaltic versus peridotitic slab sources of fluids?, *Geology*, *30*(11), 1035–1038, doi:10.1130/0091-7613(2002)030<1035:ATRVIC>2.0.CO;2.

Saltzer, R. L., R. D. van der Hilst, and H. Karason (2001), Comparing P and S wave heterogeneity in the mantle, *Geophys. Res. Lett.*, *28*(7), 1335–1338, doi:10.1029/2000GL012339.

Scherbaum, F. (2002), Analysis of digital earthquake signals, in *International Handbook of Earthquake and Engineering Seismology*, pp. 349–355, Academic, Boston, Mass.

Syracuse, E. M., and G. A. Abers (2006), Global compilation of variations in slab depth beneath arc volcanoes and implications, *Geochem. Geophys. Geosyst.*, *7*, Q05017, doi:10.1029/2005GC001045.

Syracuse, E. M., G. A. Abers, K. M. Fischer, P. E. van Keken, E. A. Kneller, and C. A. Rychert (2007), Improving seismic constraints on subduction zone geometry, *Eos Trans. AGU*, *88*(52), Fall Meet. Suppl., Abstract T43C-06.

Takei, Y. (2002), Effect of pore geometry on V_P/V_S: From equilibrium geometry to crack, *J. Geophys. Res.*, *107*(B2), 2043, doi:10.1029/2001JB000522.

Tarantola, A. (1986), A strategy for nonlinear elastic inversion of seismic reflection data, *Geophysics*, *51*(10), 1893–1903, doi:10.1190/1.1442046.

Tarantola, A., and B. Valette (1982), Generalized nonlinear inverse problems solved using the least squares criterion, *Rev. Geophys.*, *20*(2), 219–232, doi:10.1029/RG020i002p00219.

Thurber, C. H. (1992), Hypocenter velocity structure coupling in local earthquake tomography, *Phys Earth Planet Inter*, *75*(1–3), 55–62, doi:10.1016/0031-9201(92)90117-E.

van der Hilst, R. D., and E. R. Engdahl (1992), Step-wise relocation of ISC earthquake hypocenters for linearized tomographic imaging of slab structure, *Phys. Earth Planet Inter.*, *75*(1–3), 39–53, doi:10.1016/0031-9201(92)90116-D.

Vidale, J. E. (1990), Finite-difference calculation of traveltimes in 3 dimensions, *Geophysics*, *55*(5), 521–526, doi:10.1190/1.1442863.

Wade, J. A., T. Plank, E. Hauri, K. Roggensack, and K. Kelley (2006), Prediction of arc magma water contents via measurement of H_2O in clinopyroxene, *Eos Trans. AGU*, *87*(52), Abstract V53E-07.

Watson, E. B., and A. Lupulescu (1993), Aqueous fluid connectivity and chemical-transport in clinopyroxene-rich rocks, *Earth Planet. Sci. Lett.*, *117*(1–2), 279–294, doi:10.1016/0012-821X(93)90133-T.

Zelt, C. A. (1998), Lateral velocity resolution from three-dimensional seismic refraction data, *Geophys. J. Int.*, *135*, 1101–1112, doi:10.1046/j.1365-246X.1998.00695.x.

Zhao, D., Z. Wang, N. Umino, and A. Hasegawa (2007), Tomographic imaging outside a seismic network: Application to the Northeast Japan Arc, *Bull. Seismol. Soc. Am.*, *97*(4), 1121–1132, doi:10.1785/0120050256.